Microearthquakes on the Endeavour segment of the Juan de Fuca Ridge

William S. D. Wilcock and Stephen D. Archer
School of Oceanography, University of Washington, Seattle, Washington, USA

G. M. Purdy[1]
Department of Geology and Geophysics, Woods Hole Oceanographic Institution, Woods Hole, Massachusetts, USA

Received 28 February 2001; revised 13 December 2001; accepted 18 December 2001; published 11 December 2002.

[1] We report the results of a 55-day microearthquake experiment on the Endeavour segment of Juan de Fuca Ridge. The network covered a 5-km section of the ridge axis centered on the Main vent field and extended 15-km off axis on the west flank. The ridge axis and flanks were seismically active, and 1750 earthquakes were located with a minimum of five travel time picks including at least one *S* wave. Over half the earthquakes occurred in swarms, and a waveform cross-correlation technique was used to obtain relative locations. On the western flank, the hypocenters for four swarms at midcrustal depths are compatible with steeply dipping fault planes that strike at 035–050°N and oblique to the abyssal hills. Focal mechanisms determined from *P* wave first motions and *P*/*S* amplitude ratios are predominantly strike-slip with north-south compression and appear to be affected by the reorganization of the Explorer plate. Earthquakes beneath the ridge axis are concentrated in a band of intense seismicity at 1.5–3.5 km depth. To the north of High Rise vent field, the seismicity defines a plane striking parallel to the ridge axis and dipping east at 70° and the earthquakes appear to extend beneath an axial reflector previously imaged at 2.3 km depth. Farther south, the hypocenters are not compatible with a single fault plane. Focal mechanisms are characterized by subhorizontal tension axes oriented in all directions except parallel to the ridge and suggest a stress field that is about equally influenced by ridge spreading and hydrothermal cooling. *INDEX TERMS:* 3035 Marine Geology and Geophysics: Midocean ridge processes; 7230 Seismology: Seismicity and seismotectonics; 7215 Seismology: Earthquake parameters; 7220 Seismology: Oceanic crust; *KEYWORDS:* mid-ocean ridge, microearthquake

Citation: Wilcock, W. S. D., S. D. Archer, and G. M. Purdy, Microearthquakes on the Endeavour segment of the Juan de Fuca Ridge, *J. Geophys. Res.*, *107*(B12), 2336, doi:10.1029/2001JB000505, 2002.

1. Introduction

[2] One paradigm of mid-ocean ridge research is that the morphology and seismicity of spreading centers is determined by spreading rate and magma supply. On slow spreading ridges or ridges with low levels of mantle melt production, there is insufficient melt to support a steady state axial magma chamber. Hydrothermal circulation cools the lower crust on axis and a significant proportion of extension occurs on large inward facing normal faults leading to the formation of a deep axial valley. As a result, the largest earthquakes are observable at teleseismic distances and short microearthquake experiments record many events. In contrast, on faster spreading ridges or ridges with high melt supply, a steady state axial magma chamber (AMC) often exists at midcrustal depths and the underlying crust is near or above the solidus. Extension occurs predominantly by magmatism and the ridge axis is characterized by a gentle high. There are no teleseismic earthquakes and the ridge is nearly aseismic except during short intervals surrounding diking-eruptive events.

[3] At intermediate spreading rates, global observations [*Small and Sandwell*, 1989] and thermal models [*Phipps Morgan and Chen*, 1993] suggest that the transition between the two states is very sensitive to small changes in spreading rate or magma supply. One example is the difference between the Gorda Ridge and the Juan de Fuca Ridge (JdFR) [*Hooft and Detrick*, 1995]. Both have spreading rates of $\sim$6 cm yr^{-1} but they appear quite different. The Gorda Ridge has a deep axial valley, and it supports many moderately sized earthquakes. Gravity data suggest that the crust is slightly thicker on the JdFR probably because magma supply is enhanced by the presence of Axial Seamount [*Hooft and Detrick*, 1995]. Away from this seamount the axial bathymetry is fairly muted and most segments are only seismically active during eruptions.

[1]Now at Lamont-Doherty Earth Observatory, Palisades, New York, USA.

0148-0227/02/2001JB000505$09.00

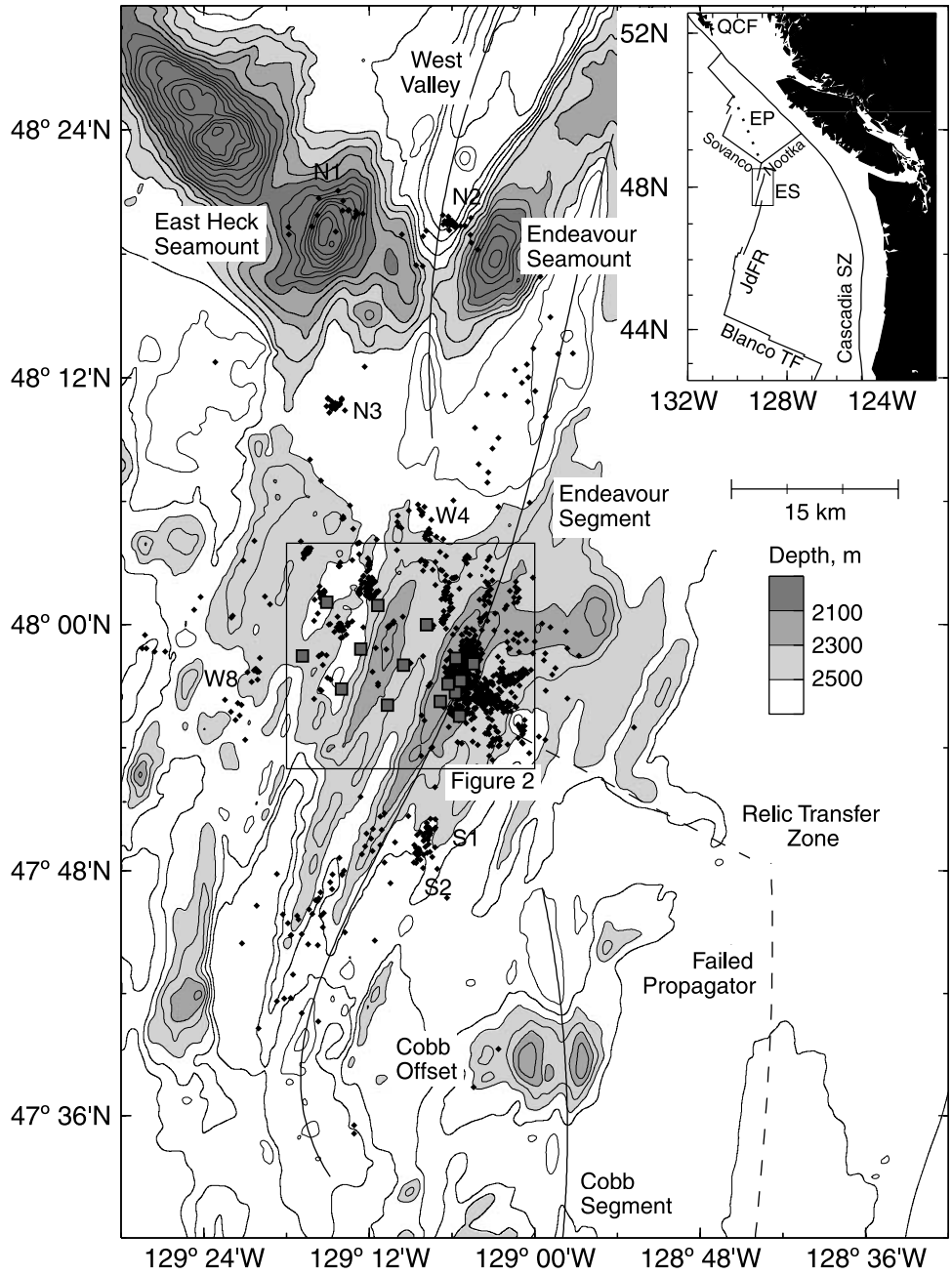

Figure 1. SeaBeam bathymetric map of the Endeavour segment, contoured at 100-m intervals, showing the location of ocean bottom seismometers (gray squares) and epicenters determined using HYPOINVERSE [*Klein*, 1978] (black diamonds). Labeled solid lines show the location of the ridge axis, and dashed lines show a failed propagator on the Cobb segment and a relict transfer zone that previously connected the Cobb and Endeavour segments [*Johnson et al.*, 1983]. A box delineates the area covered by Figure 2. Swarms listed in Table 2 that are located outside this area are also labeled. The inset shows the regional location of the experiment. Plate boundaries are shown by solid lines with a dotted line showing the proposed location of the incipient Explorer transform zone [*Rohr and Furlong*, 1995; *Kreemer et al.*, 1998]. The label notation is as follows: ES, Endeavour segment; EP, Explorer plate; JdFR, Juan de Fuca Ridge; SZ, subduction zone; and TF, transform fault.

[4] The Endeavour segment (Figure 1) at the northern end of the JdFR is an exception to this simple relationship between morphology and seismicity. Its bathymetry is similar to other segments on the JdFR, but the levels of seismicity are much higher and comparable to the Gorda Ridge. Data from land-based networks and nearly 10 years of earthquake monitoring with the U.S. Navy's Sound Surveillance System (SOSUS) [*Dziak and Fox*, 1995; *Johnson et al.*, 2000] show that the Endeavour region hosts earthquakes up to magnitude 4. Several small ocean bottom

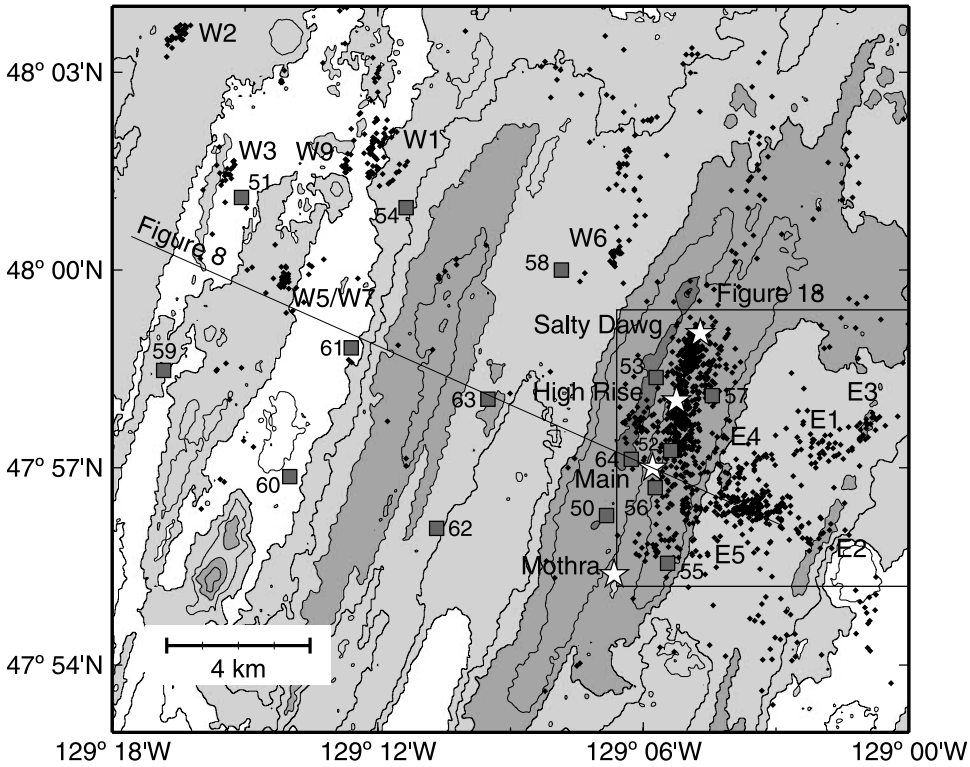

Figure 2. SeaBeam bathymetric map of the experiment region (contoured at 100-m intervals with depths shaded as in Figure 1) showing the location of OBSs (labeled gray squares), epicenters (diamonds), and four high-temperature vent fields (labeled white stars). Swarms listed in Table 2 are also labeled. A box delineates the area covered by Figure 18.

seismometer (OBS) deployments show that the ridge axis is continuously active at lower magnitude thresholds [*McClain et al.*, 1993].

[5] There are a number of observations that suggest the magmatic budget for the Endeavour segment is currently low. The ridge axis is characterized by a 1-km-wide 100-m-deep axial valley that is highly fissured and devoid of recent eruptions [*Tivey and Delaney*, 1986]. While a seismic reflection profile shows a weak axial reflector at ~2-km depth [*Rohr et al.*, 1988], a seismic tomography experiment [*White and Clowes*, 1990, 1994] shows no sign of a substantial low-velocity low-Q region underlying the reflector. The axial valley hosts at least four high-temperature vent fields [*Delaney et al.*, 1992; *Thomson et al.*, 1992] (Figure 2) with sulfide structures that are much larger than elsewhere on the JdFR. *McClain et al.* [1993] argue that active faults on the Endeavour provide long-term conduits that are necessary for the formation of mature vent fields. The high hydrothermal heat flux on the Endeavour is most easily explained if heat is being mined by a cracking front as opposed to a stationary heat uptake zone above an AMC [*Wilcock and Delaney*, 1997].

[6] The anomalous nature of the Endeavour segment is best explained by invoking a recent decline in magma supply. There are two alternative explanations for its cause. *Kappel and Ryan* [1986] argue that crustal formation along the JdFR undergoes cyclical fluctuations and that different segments are in different phases of the cycle. Episodes of constructional volcanism are followed by intervals of increased faulting that split the axial volcanic ridge and lead to the formation of inward facing abyssal hills. On the central Endeavour, these split ridges are spaced ~6 km or 200,000 years apart. If the model is correct, the segment is in the waning stages of a magmatic cycle and entering a tectonic phase. Since most segments on the JdFR are not seismically very active, it could be inferred that the tectonic phase is relatively short-lived.

[7] Alternatively, the anomalous levels of seismicity on the northern portion of the JdFR may be a result of regional tectonics. The Explorer microplate to the north (Figure 1, inset) has evolved rapidly since it detached from the Juan de Fuca plate ~5 Myr ago. The Sovanco transform fault and Nootka fault zones [*Hyndman et al.*, 1979] form the southern and eastern boundaries of the Explorer microplate, and they meet the Juan de Fuca Ridge in an unstable and poorly defined triple junction. The Sovanco is characterized by extensive block rotations within a wide zone of diffuse deformation [*Cowan et al.*, 1986] and magnetic isochrons on the Pacific plate suggest that the transform shear zone recently extended ~50–100 km farther south of its present location [*Wilson*, 1993]. Three seamount chains dominate the bathymetry south of the Sovanco and on the basis of the distribution of SOSUS epicenters, *Dziak and Fox* [1995] suggest that transform motion may be initiating along the northernmost (Heck) seamount chain. The Endeavour segment itself is offset at either end by overlapping spreading centers and a large portion of the segment appears to be a failing rift [*Karsten et al.*, 1990]. Axial lavas from the Endeavour are enriched compared to lavas obtained off axis and from the ridge axis to the south. Small-scale variations

in incompatible element compositions suggest that the central portion of the segment has received multiple parental melts. *Karsten et al.* [1990] hypothesize that these petrological characteristics may be a result of a decreased depth and extent of melting as the Endeavour rift fails.

[8] In this paper, we present the tectonic results from a microearthquake experiment that was motivated by a desire to understand the anomalously high levels of seismicity on the Endeavour and the relationships between axial seismicity and high-temperature hydrothermal circulation on the ridge axis. The data set has already been analyzed for shear wave splitting [*Almendros et al.*, 1999] and tidal triggering [*Wilcock*, 2001], and the results of tomographic studies will be reported elsewhere.

2. Microearthquake Experiment

[9] In June 1995, we deployed 15 Office of Naval Research (ONR) ocean bottom seismometers (OBSs) for 55 days on the central portion of the Endeavour segment (Figures 1 and 2). Seven OBSs were deployed in a tight network along a 5-km section of the ridge axis that includes the Main and High Rise vent fields, and the remainder were located up to 15-km off axis on the lightly sedimented west flank. The ONR OBS [*Jacobson et al.*, 1991] records data from four channels; a hydrophone on the main instrument frame and three orthogonal 1-Hz seismometers in a compact package that is deployed from a mechanical arm after the OBS is on the seafloor. Gimbaled mounts allow the seismometers to self-level provided that the package is within 15° of vertical. Each channel was sampled digitally at 128 Hz after applying an eight-pole 50-Hz antialias filter. Because of limited disk capacity, the OBSs recorded continuously for only the first 2 days and last 14 days of the experiment. For the remaining time they operated in event-detect mode, recording data only for time windows enclosing triggers when the root mean square (RMS) amplitude ratio of 1 s and 10 s running windows exceeded 3 on the vertical seismometer channel. Clock drifts averaged 0.5 ms d^{-1} and were corrected assuming linear drift.

[10] All the OBSs returned data, although OBS 54 and 62 failed after 6 and 16 days, respectively. The sensor packages for eight OBSs (50, 53, 55, 56, 57, 60, 62, and 64), including all but one of the seven deployed in the rough terrain on axis, lay at an angle of greater than 15° disabling at least one horizontal channel. One horizontal channel also failed on OBSs 61 and 63. The vertical channel on OBS 58 was noisy, and it only triggered on a small number of earthquakes when recording in event-detect mode. Average trigger rates on the other OBSs varied between 50 and 350 per day. Tests on samples of the continuously recorded data showed that the event detection algorithm triggered on all earthquakes with identifiable body waves and so we used this method to extract earthquakes from continuously recorded data. Over the entire experiment, there were 3268 occasions when four or more OBS triggered within 30 s of each other. Of these, 2623 were identified as earthquakes with at least one clear body wave arrival. Most of the remaining 645 intervals appear to result from coincident but unrelated triggers on noise, although a few examples of emergent earthquakes and biological sounds were noted.

[11] During the first 2 days of the experiment, we detonated forty-nine 4.5-kg (10 lb.) explosive shots in and around the network. We inverted water wave travel times for the location of OBSs and for horizontal coordinates and origin times of the shots [*Creager and Dorman*, 1982; *Toomey et al.*, 1985]. A total of 478 water wave arrival times were picked on the hydrophone channels for shots at ranges less than 10 km. The water velocity profile used in the inversion was obtained by smoothing a sound velocity profile calculated with CTD data collected during the deployment by other researchers [*Veirs et al.*, 1999]. The shot depths were fixed to values determined from the bubble pulse frequency. The initial estimates of the shot coordinates and origin times were obtained from Global Positioning System (GPS) fixes and shipboard recordings, respectively. The initial estimates of the OBS locations were obtained from GPS fixes at the drop sites with depths read from a SeaBeam map. The RMS travel time residual after the inversion was 6 ms, and the average standard deviation in OBS horizontal positions was 12 m.

3. Methods

3.1. Arrival Time Data

[12] We first picked *P* and *S* arrivals manually. In order to repick or eliminate erroneous arrival times efficiently, we employed an iterative scheme. After picking each event, HYPOINVERSE [*Klein*, 1978] was used to obtain a preliminary location with a four-layer velocity model. The seismograms were displayed with travel time picks and predictions, and if necessary, the picks were adjusted and the process repeated. Rather than assigning relative errors to each pick, we chose to eliminate picks for a particular event if we judged that the reading error was clearly much larger than for the same phase at other stations. In order not to bias the arrival time data, we made a concerted effort to pick each phase consistently and avoided making small adjustments on the basis of residuals alone. Many *S* waves for earthquakes in the axial region are quite emergent, and our approach was to pick ambiguous arrivals at the earliest plausible time. Since the majority of *S* waves were not recorded on two well-leveled horizontal channels, it is possible that *S*-to-*P* conversions at the base of layer 2A have been misidentified as *S*. The total data set comprised 9046 *P* wave picks and 6097 *S* wave picks.

[13] Many of the earthquakes occurred in swarms. Because closely spaced earthquakes often generate similar waveforms at a given station, cross-correlation techniques can be used to generate a set of self-consistent travel time picks whose relative errors are much smaller than the absolute errors of individual picks. *Shearer* [1997] describes a method whereby the differential delays obtained by cross-correlating event pairs are combined with the original travel time picks by inverting for a set of adjusted picks at each station that minimizes the misfit to both the original picks and the differential times.

[14] We adopted a similar approach. We applied a 20 Hz low-pass filter and calculated cross correlations in the time domain on the 128-Hz records. Unlike *Shearer* [1997], the cross correlations were limited to earthquakes whose HYPOINVERSE epicenters were located within 2 km of each other. For *P* waveforms, the relative delay was obtained by

cross correlating 0.2- to 0.3-s-long windows with a maximum time shift of 0.1 s. We used the vertical seismometer channel except for three OBS (55, 58, and 61) where the hydrophone channel had better signal to noise. The delay times were estimated from the maximum of the absolute values of the cross correlation. Using absolute values allows for the possibility that the polarities of two waveforms are opposite, a result that can also be confirmed by the zero-frequency intercept of the cross spectrum [*Nakamura*, 1978]. For *S* waves, we used 0.5- to 0.7-s-long windows and a maximum time shift of 0.25 s. When both horizontal seismometer channels were available, we summed the absolute values of the cross-correlation function; if neither horizontal channel was available, we used the vertical. For both *P* and *S* waveforms, we rejected delays if the absolute value of the correlation coefficient was less than 0.7. Other researchers have found that waveform cross correlations obtained in the frequency domain can be used to obtain relative delays whose precision is substantially smaller than sample interval [*Poupinet et al.*, 1984; *Waldhauser et al.*, 1999]. We experimented with this technique, but it produced little improvement in the delay time misfits. There are several possible causes. The short length of windows and the small bandwidth of many waveforms will limit the precision of spectral alignments. The timing errors in our data may be too large to support the technique. For some swarms, the waveforms may not be sufficiently similar.

[15] For many OBSs the *S* waveform is quite narrowband, and cycle skipping and polarity errors caused problems. Because this leads to outlying residuals when the differential delays are inverted for adjusted picks, we used an iterative approach to automatically correct erroneous delays [*VanDecar and Crosson*, 1990]. Manual intervention was often required to fix alignments and eliminate ambiguous waveforms.

[16] We applied this method separately to 18 earthquake clusters lying off the ridge axis and all the microearthquakes located in the axial region. We analyzed 1266 earthquakes and were able to use cross correlations to constrain 5463 *P* and 2934 *S* picks. A total of 889 earthquakes have at least five cross-correlation pick times.

3.2. Hypocentral Locations

[17] All the microearthquakes were located using HYPOINVERSE [*Klein*, 1978] which iteratively solves the nonlinear problem of determining the hypocenter and origin time by performing a singular value decomposition of the travel time partial derivative matrix and calculating the generalized inverse. The algorithm assumes a one-dimensional layered velocity model and a constant V_P/V_S ratio. Arrival time picks can be weighted according to the quality of the observation and outlying travel times are excluded from the final solution. Step-length damping stabilizes the iterations and an eigenvalue cutoff is employed to prevent the solution moving in directions that are poorly constrained by the data. To account for structure beneath each receiver, shallow variations in V_P/V_S [*Collier and Singh*, 1998; *Barclay et al.*, 2001], and biases in *S* wave picks, we incorporated independent station corrections for *P* and *S* arrivals.

[18] We used a 33-layer crustal *P* wave velocity model based on the average upper crustal velocity structure obtained by an earlier refraction experiment [*Cudrack and Clowes*, 1993] with a Moho depth estimated from reflection data [*Rohr et al.*, 1988] (Figure 3). We employed two methods to estimate the V_P/V_S ratio. First, when both *P* and *S* wave picks were available for an earthquake on two receivers, we calculated the *S* arrival time difference, ΔS, and *P* arrival time difference, ΔP. The slope of a linear fit to a plot of ΔS values versus the corresponding ΔP yields an estimate of V_P/V_S [*Francis*, 1976]. When applied to data from individual station pairs, this technique yielded highly variable V_P/V_S values from 1.6 to 2.0, a result that suggests that there may be considerable heterogeneity in Poisson's ratio in our region. The full data set for all station pairs comprises 5633 points, and a linear regression yielded $V_P/V_S = 1.84$ (Figure 4a).

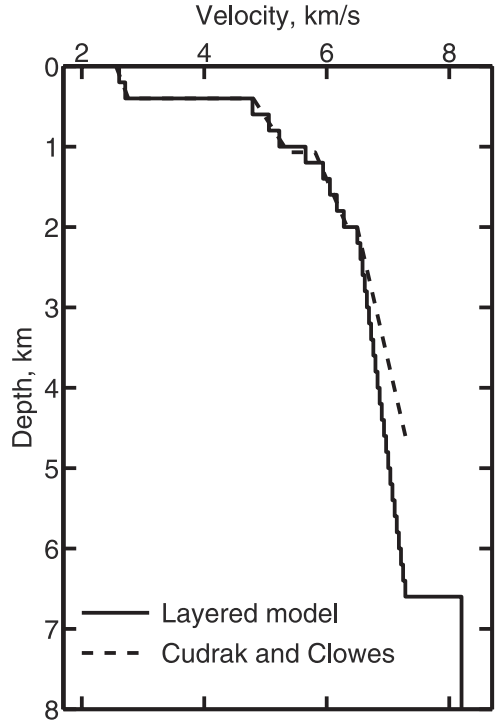

Figure 3. The 33-layer *P* wave velocity model used to locate the microearthquakes (solid line) and the crustal model derived from refraction data by *Cudrak and Clowes* [1993] (dashed line).

[19] Second, we considered a subset of 437 earthquakes with at least eight good quality picks and epicenters within 3 km of the nearest OBS. We located these earthquakes assuming a range of V_P/V_S ratios. To account for their greater picking uncertainty, *S* arrival times were ascribed a weight of 0.5. For each V_P/V_S ratio, we iteratively solved for independent *P* and *S* station delays so as to reduce the mean travel time residual at each station to zero. An arrival time error σ can be estimated [*Sohn et al.*, 1998b] by

$$\sigma^2 = \frac{\sum_{i=1}^{n} \sum_{j}^{m_i} w_{i,j}^2 \Delta t_{i,j}^2}{\sum_{i=1}^{n} (m_i - 4)}, \qquad (1)$$

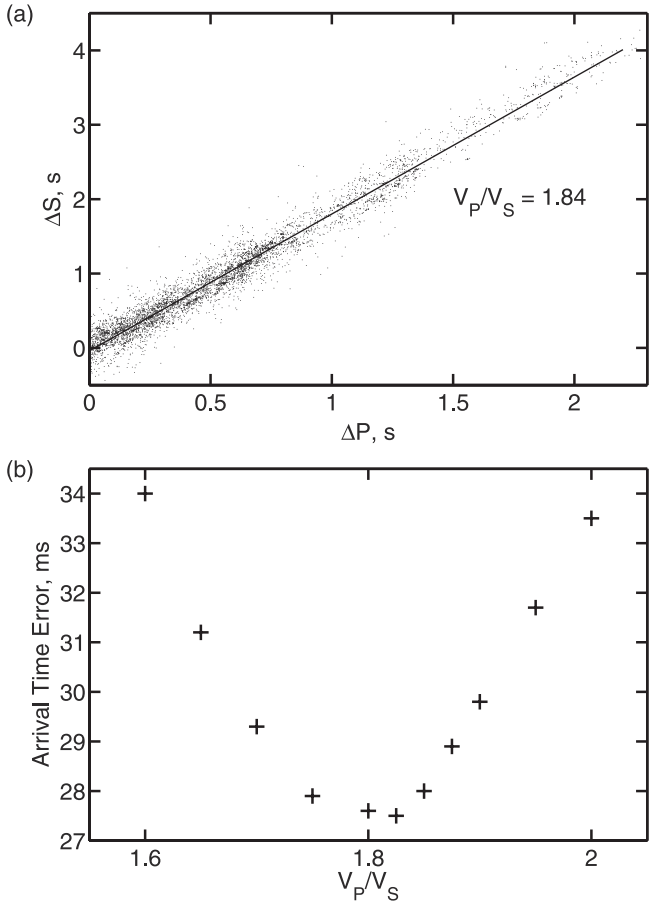

Figure 4. (a) Plot of differential *S* wave times against differential *P* wave times for all combinations of earthquake pairs and station pairs recording both phases. A straight-line fit to the data has a slope V_P/V_S = 1.84. (b) Plot of the estimated arrival time error (equation (1)) versus the assumed V_P/V_S for 437 earthquakes with at least 8 picks and epicenters less than 3 km from the nearest OBS (for V_P/V_S = 1.85). The minimum error is obtained for V_P/V_S = 1.825.

where n is the number of earthquakes, m_i is the number of picks for the ith earthquake, $w_{i,j}$ is the weigh ascribed to the jth pick, and $\Delta t_{i,j}$ is its travel time misfit. A plot of the estimated arrival time error against V_P/V_S has a minimum of 28 ms at V_P/V_S = 1.83.

[20] To locate the full data set, we used V_P/V_S = 1.83 and station delays that were obtained from the subset of well-recorded events described above (Table 1). *S* arrivals were again assigned a weight of 0.5, a value that is consistent with the residuals. Because the picks constrained by cross correlations have smaller reading errors, we downweighted manual picks by a factor of 0.5 for earthquakes where both types of picks were included in the solution. The depth control is generally poor for earthquakes located more than 3 km from the nearest OBS, and so for these events we fixed the depth to 3 km. After discarding earthquakes with RMS residuals exceeding 0.1 s, a total of 1899 earthquakes were located of which 1750 have a minimum of one *S* wave and five total picks.

[21] As noted above, the differential arrival times obtained by cross-correlating waveforms recorded at one station are considerably more accurate than the absolute picks. Furthermore, differential times for closely spaced events are relatively insensitive to errors in the velocity model because the ray paths are similar. Multiple event relocation procedures can be used to obtain greatly improved relative locations for earthquake clusters. In this study we implemented the hypocentroidal decomposition method [*Jordan and Sverdrup*, 1981] to determine the hypocentroid (average event location) and the cluster vector (the deviations of individual hypocenters) and their uncertainties. Unlike the HYPOINVERSE locations, the *P* and *S* wave picks were assigned equal weight in the relative relocations because the cross-correlation alignments are equally accurate and the cluster vector is relatively insensitive to the higher uncertainty of the *S* wave velocity model. We limit the relocations to earthquakes with at least five cross-correlated picks, since this provides the redundant information necessary to identify misaligned arrivals.

[22] The cluster vector is calculated using travel time partial derivatives calculated at the hypocentroid. As the distance of hypocenters from the hypocentroid increases, biases due to nonlinearity will increase. With the exception of some distant swarms, individual cluster hypocenters are generally located no more than ~0.75 km from the hypocentroid, but even at these small distances the biases can be noticeable. For each swarm that we located with this method we used synthetic tests to estimate the location biases and ensure that the primary characteristics of the swarm distribution were well resolved.

3.3. Source Parameters

[23] First motion *P* wave polarities are commonly used to determine double-couple focal mechanisms for marine microearthquake studies. However, since the number of stations is relatively small, solutions can generally only be determined for a handful of events. For our study, *P* wave polarities alone are sufficient to determine unique double-couple solutions for ~100 earthquakes. However, well over half of these solutions are not robust; a single misidentified

Table 1. Station Corrections[a]

	P Waves		*S* Waves	
Instrument	Δt_P, s	N_P	Δt_S, s	N_S
50	0.00	261	−0.09	323
51	0.01	111	−0.22	125
52	−0.01	291	−0.24	263
53	0.03	311	−0.10	251
54	−0.03	17	−0.18	18
55	−0.08	111	−0.42	16
56	−0.01	214	−0.14	13
57	−0.05	204	−0.35	11
58	0.02	7	−0.01	22
59	0.08	116	−0.09	216
60	0.02	105	−0.15	130
61	0.01	17	−0.23	15
62	0.06	5	0.15	3
63	0.00	324	−0.10	315
64	0.00	222		0
Mean	0.00		−0.14	

[a]Symbol definitions are Δt, station correction in seconds (corrections are added to the observed arrival time), and N, number of observations used to calculate the correction. The mean station corrections in the final row have been weighted by the number of observations. The *P* wave corrections have been adjusted so that the weighted mean is zero.

polarity or small errors in the ray takeoff directions can change the solution significantly.

[24] Because the radiation patterns of *P* and *S* waves are different, *P* to *S* wave amplitude ratios can provide strong constraints on focal mechanisms. *Shen et al.* [1997] describe a method to incorporate this information into double-couple solutions derived from marine microearthquake data. The amplitudes of the *P* and *S* waves are read from the maximum peak-to-peak amplitude in the first two cycles after their onset on the vertical and horizontal components, respectively. For each station the observed distribution of the *P* to *S* amplitude ratios is compared to the predicted distribution assuming that they randomly sample the focal sphere and that the *P* and *S* waves have the same takeoff direction (i.e., constant V_P/V_S). *Shen et al.* [1997] find that the observed and predicted distributions have similar shapes but are generally offset from each other. This is presumably due to differences in *P* and *S* wave attenuation and uncertainties in channel gains, seismometer coupling, and the velocity structure beneath the station. They determine an empirical correction factor for each station to align the observed amplitude ratios with the predictions. A grid search method is then used to find the double-couple solution that satisfies all the *P* wave polarity constraints and minimizes the misfit to the corrected amplitude defined by

$$R_a = \frac{\sum_{i=1}^{m} W_i \left[\ln(P_O/S_O)_i - \ln(P_C/S_C)_i\right]^2}{\sum_{i=1}^{m} W_i}, \qquad (2)$$

where (P_O/S_O) is the observed and corrected *P/S* ratio, (P_C/S_C) is the calculated ratio, *W* is the weight given to the observation, and *i* is the index of *m* amplitude ratios.

[25] We used a similar technique. Because the *S* wave picks for some OBS may be biased early, the *S* amplitudes were calculated from four cycles. All amplitudes were corrected using the incidence angle determined from HYPOINVERSE. Only four OBS returned good data from all three seismometer channels. OBS 58 had a noisy vertical channel, so we calculated *P/S* ratios from the horizontal channels. For the ten OBSs with incomplete horizontal data, we calculated *P/SV* ratios from the vertical channel. Like *Shen et al.* [1997], we found that the shape of the observed distribution of *P/S* or *P/SV* amplitudes matched the predictions reasonably well (Figure 5). There were noticeably fewer observations on the tails of the distribution probably due to effects of background noise, scattered energy, and secondary arrivals. For OBS 50, the distribution of *P/SV* amplitudes fit the predicted distribution well, but for unknown reasons the corrected *P/SV* amplitudes were nearly always inconsistent with other data. We discarded amplitude ratios for this instrument.

[26] To account for variable uncertainties in the amplitude ratios, we minimized the following objective function:

$$R_a = \sum_{i=1}^{m} \frac{\left[\ln(P_O/S_O)_i - \ln(P_C/S_C)_i\right]^2}{\left[(N_O/P_O)_i^2 + (N_O/S_O)_i^2\right] + \left[\ln(P_C/S_C)_i^{\max} - \ln(P_C/S_C)_i^{\min}\right]^2}. \qquad (3)$$

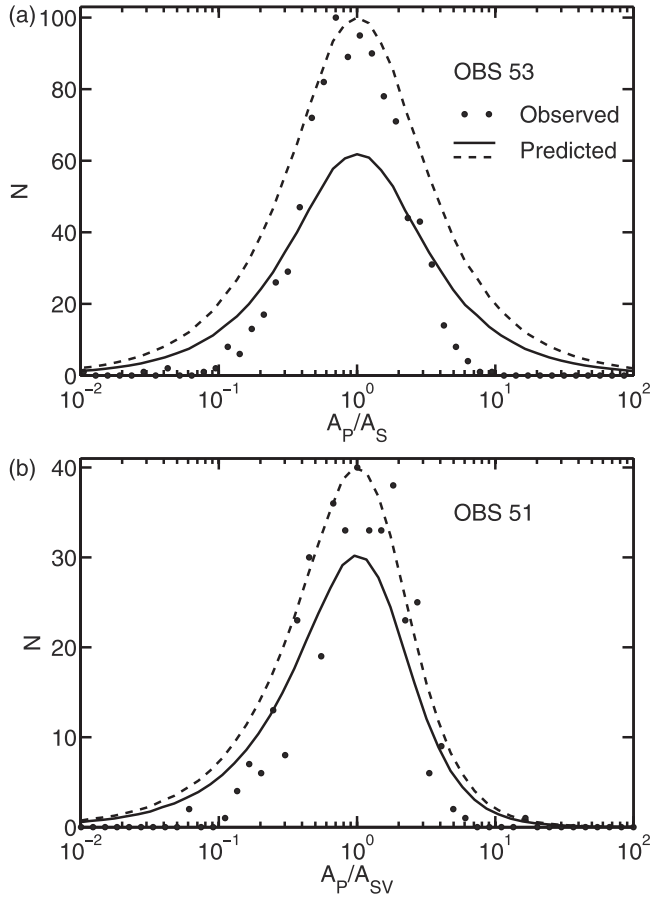

Figure 5. (a) Observed (solid circles) and predicted (lines) frequency distributions of *P* to *S* amplitudes for OBS 53. Following *Shen et al.* [1997], the predictions assume that the *P* and *S* waves randomly sample the focal sphere and the observations have been shifted horizontally so that they align with the predictions. The predictions are shown normalized to the maximum observed earthquake frequency (dashed) and to the number of observations (solid). (b) As for Figure 5a except *P* to *SV* amplitudes are shown for OBS 51.

The first term in the denominator is an approximate estimate of the uncertainty in the observed *P/S* ratio based on N_O, the maximum peak-to-peak amplitude of a noise sample taken prior to the *P* arrival. The second term in the denominator accounts for uncertainties in the ray takeoff direction by searching for the maximum, $(P_C/S_C)^{\max}$, and minimum, $(P_C/S_C)^{\min}$, calculated amplitude ratios within a 10° cone centered about the takeoff direction predicted by HYPOINVERSE. This term is particularly important when using *P/SV* ratios because the nodal points for *SV* fall on the nodal planes for *P* and the amplitude ratio in the vicinity of the nodal points is very sensitive to uncertainties in the takeoff direction.

[27] We analyzed ~250 earthquakes located within or near the network and with at least 5 clear polarity picks and 3 amplitude ratios. For each event, we searched first for a solution that minimized the objective function and satisfied the polarities. Because *P* wave polarities are difficult to pick

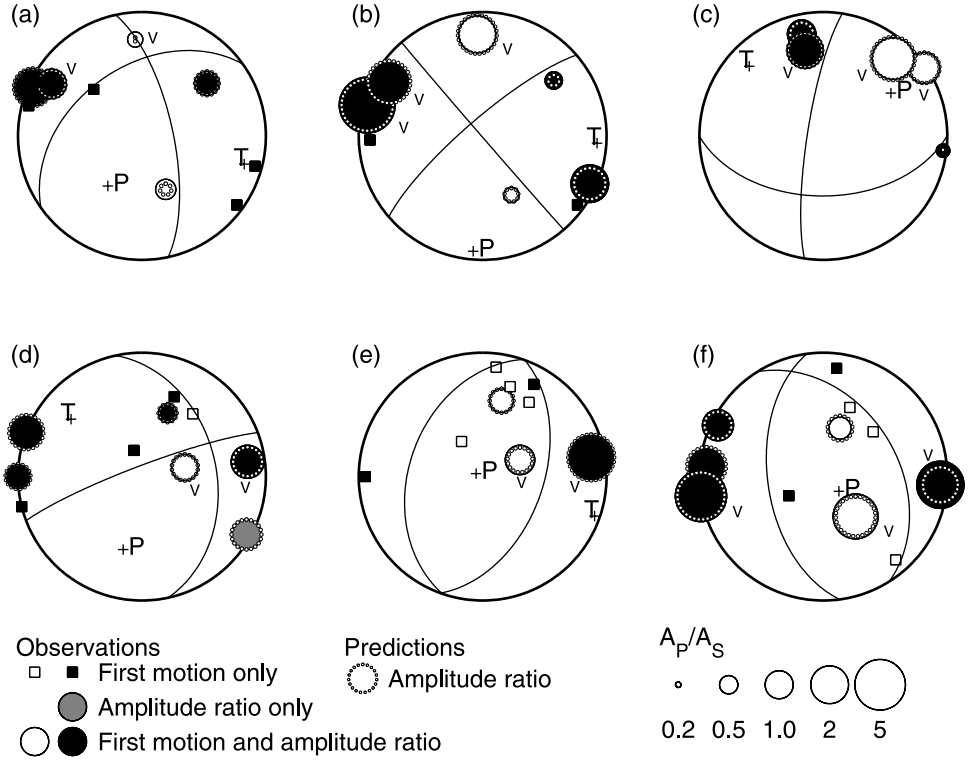

Figure 6. Examples of fault plane solutions showing focal planes (solid lines) and tension (*T*) and pressure (*P*) axes determined from *P* wave first motions and *P/S* amplitude ratios using a method based on work by *Shen et al.* [1997] (see text). Arrivals with *P/S* amplitude ratios are plotted as circles with a diameter proportional to the logarithm of the observed amplitude ratio; arrivals labeled "V" are P/SV amplitude ratios determined from the vertical channel. The predicted amplitude ratios of the best fitting double-couple solution are shown as dotted circles. Arrivals with first motion data only are shown as squares. Compressional and dilatational arrivals are shown by filled and open symbols, respectively. Solutions are shown for off-axis earthquakes: (a)–(b) swarm W5 and (c) swarm W6; and for axial earthquakes (d) in swarm A1, (e) in swarm A4, and (f) between the Main and High Rise vent fields.

near nodal planes and there are uncertainties in the takeoff direction, we accepted misfiting polarities if the radiation factor was less than 0.1. We inspected the objective function to ensure that polarities and amplitudes could not be fit acceptably with a substantially different mechanism. We then searched for alternative solutions with up to two misfiting polarities. If we could get a better fit to the amplitude ratios and the mechanism was substantially different, we reinspected the seismograms to determine whether the misfiting first motions should be considered robust. We only accepted solutions if we could find a unique mechanism with an acceptable misfit ($R_a < m$). We were able to determine focal mechanisms for 173 earthquakes. Figure 6 shows examples of solutions for six events. In general, the amplitude ratios are matched quite well and the inclusion of amplitude data clearly improves the solutions.

[28] We estimated the seismic moment for all located earthquakes using the low-frequency displacement spectra of *P* and *S* waves [*Tréhu and Solomon*, 1983; *Toomey et al.*, 1988]. For each earthquake the moment was obtained by averaging the values calculated on all OBSs with good quality records. *S* wave corner frequencies were used to estimate fault radii, displacements, and stress drops for selected earthquakes [*Brune*, 1970].

4. Results

[29] High levels of seismicity were observed during the experiment both on and off axis and many of the earthquakes occurred in swarms (Table 2). Figure 7 shows a time histogram of the number of located earthquakes. The earthquake count in 12-hour intervals varies from 2 to 77. Of 1750 earthquakes located with at least one *S* wave pick and five total picks, focal depths have been determined for 1134 that lie within 3 km of the nearest station. Over half (670) of these proximal earthquakes are located within 1.5 km of the spreading axis. These axial earthquakes are concentrated in a band of intense seismicity at depths of 1.5 to 3.5 km (Figure 8) that extends several kilometers to the north of the Main vent field (Figure 2). A significant number of earthquakes are located to the east of the ridge axis including a band of earthquakes that extends ~5-km east-southeast of the Main vent field. To the west of the ridge axis, the seismicity is dominated by swarms, mostly located to the north of the network and up to 20 km off axis. Well-

Table 2. Swarm Parameters[a]

ID	Date	Duration, hours	Longitude, W	Latitude, N	Depth, km	Region	N	N_L,	σ_C, ms	$(M_0)_{max}$, N m	$\Sigma(M_0)$, N m	Point Source
W1	10 June	97	129°12.0′	48°01.9′	2.7	west	79	55	7	3×10^{12}	1×10^{13}	n
W2	11 June	39	129°16.5′	48°03.7′	(3.0)	west	30	28	5	6×10^{11}	3×10^{12}	n
A1	12 June	119	129°04.6′	47°58.5′	3.1	axial	37	18	8	3×10^{11}	2×10^{12}	n
E1	13 June	5	129°01.9′	47°57.3′	(3.0)	east	30	22	8	6×10^{11}	3×10^{12}	n
A2	14 June	85	129°05.2′	47°57.6′	2.7	axial	51	28	11	3×10^{11}	9×10^{11}	n
N1	17 June	1	129°14.5′	48°21.1′	(3.0)	north	17	5	10	5×10^{13}	8×10^{13}	y
W3	18 June	130	129°15.5′	48°01.7′	2.8	west	21	17	3	1×10^{11}	7×10^{11}	n
N2	19 June	8	129°06.3′	48°19.7′	(3.0)	north	47	23	10	2×10^{13}	4×10^{13}	y
W4	20 June	123	129°07.6′	48°04.4′	(3.0)	west	13	9	7	4×10^{12}	5×10^{12}	n
A3	23 June	48	129°05.1′	47°57.2′	3.1	axial	23	14	12	3×10^{11}	7×10^{11}	n
A4	27 June	28	129°04.9′	47°58.8′	2.3	axial	78	52	8	2×10^{12}	7×10^{12}	n
A5	30 June	5	129°05.0′	47°58.6′	2.5	axial	101	72	9	3×10^{12}	1×10^{13}	n
W5	7 July	6	129°14.2′	48°00.0′	3.5	west	11	9	4	4×10^{10}	1×10^{11}	n
S1	8 July	2	129°07.8′	47°49.3′	(3.0)	south	30	18	15	3×10^{12}	8×10^{12}	y
E2	8 July	16	129°02.3′	47°56.2′	(3.0)	east	32	21	4	6×10^{11}	2×10^{12}	y
W6	12 July	20	129°06.5′	48°00.4′	3.2	west	41	23	8	1×10^{11}	9×10^{11}	y
E3	12 July	3	129°00.8′	47°57.5′	(3.0)	east	36	24	9	4×10^{11}	2×10^{12}	y
A6	12 July	1	129°05.4′	47°55.8′	3.3	axial	38	10	7	8×10^{10}	3×10^{11}	y
E4	14 July	22	129°03.6′	47°57.0′	(3.0)	east	19	12	13	2×10^{11}	6×10^{11}	n
A7	15 July	1	129°05.9′	47°57.7′	2.3	axial	31	6	5	5×10^{10}	2×10^{11}	n
W7	17 July	9	129°14.3′	47°59.9′	3.8	west	38	31	4	1×10^{12}	3×10^{12}	n
W8	17 July	179	129°20.5′	47°57.7′	(3.0)	west	14	8	6	1×10^{11}	4×10^{11}	y
N3	24 July	33	129°14.6′	48°10.8′	(3.0)	north	28	21	6	8×10^{11}	3×10^{12}	y
W9	25 July	18	129°12.6′	48°01.6′	3.3	west	16	15	3	2×10^{11}	9×10^{11}	n
E5	25 July	188	129°03.3′	47°56.4′	(3.0)	east	128	67	10	6×10^{11}	4×10^{12}	y
S2	29 July	7	129°08.5′	47°48.9′	(3.0)	south	37	20	15	1×10^{13}	2×10^{13}	n

[a]Definitions are as follows: date and duration, day of onset in universal time (UT) and length of the shortest interval containing two-thirds of the earthquakes in the swarm; latitude, longitude, and depth, location of the swarm hypocentroid (depths in parentheses indicate that the depth was held fixed during the relocation); N, number of earthquakes in the swarm; N_L, number of earthquakes that have been relocated (a minimum of five cross-correlated times is used to relocate an earthquake); σ_C, normalized travel time misfit of the cluster vector in milliseconds (see equation (81) of *Jordan and Sverdrup* [1981]); $(M_0)_{max}$, seismic moment of the largest earthquake in the swarm; $\Sigma(M_0)$, total seismic moment release of the swarm; point source, y (yes) and n (no) indicate whether or not the 95% confidence limits for the cluster vectors are compatible with a point source for the swarm.

resolved focal depths lie at midcrustal depths (Figure 8). Swarms are also located farther afield both to the south near the axis of the Endeavour segment and to the north near West Valley and the East Heck and Endeavour Seamounts (Figure 1).

[30] Earthquake moments varied from 10^9 to 4×10^{13} N m and the total moment release for located earthquakes was 3.5×10^{14} N m. The cumulative moment releases for individual swarms are not generally dominated by a single event and the temporal distributions of moments show no consistent patterns. Seventy percent of the moment release occurred in distal events; proximal earthquakes on the ridge axis account for 12%. The four largest earthquakes and 45% of the total moment release occurred well to the north of the network near Middle Valley. Many of these earthquakes are part of swarms, N1 and N2 (Figure 1 and Table 2) on 17 June and 19 June. To the south of the network, the southern portion of the Endeavour segment near the northern end of the Cobb offset accounts for 12% of the moment release. Swarm S2 (Table 2) on 29 July accounts for half this moment release. The b value estimates (Figure 9) are close to unity and are thus more typical of tectonic than volcanic earthquakes.

[31] About half the earthquakes with moments greater than 10^{11} N m displayed clear corner frequencies between 10 and 25 Hz, implying fault radii of 50–100 m. Corresponding values for coseismic slip and average stress drop are 0.3–10 mm and 0.1–10 MPa (1–100 bars), respectively. The remainder of the larger earthquakes and a large majority of the smaller earthquakes that we inspected do not display a clear corner frequency. One interpretation is that the corner frequencies for these events are too high to be visible above background noise in the attenuated waveforms.

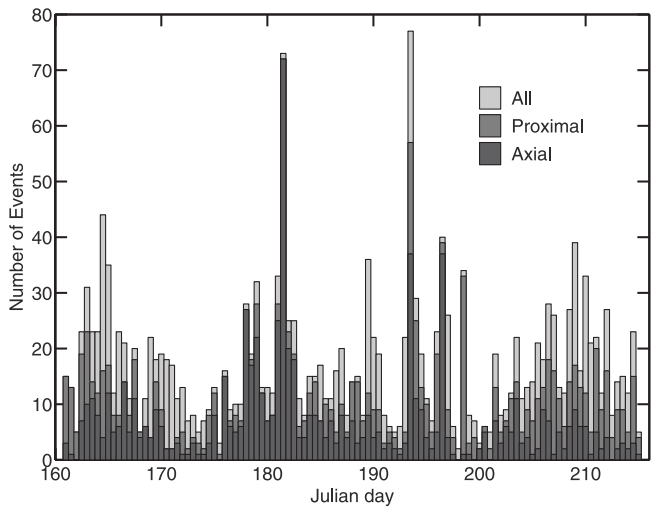

Figure 7. Histogram showing the number of located earthquakes in 12-hour periods. Subdivisions show the distribution of "proximal" earthquakes whose epicenters are within 3 km of the nearest OBS, and "axial" earthquakes whose epicenters are within 1.5 km of the ridge axis and 3 km of the nearest OBS.

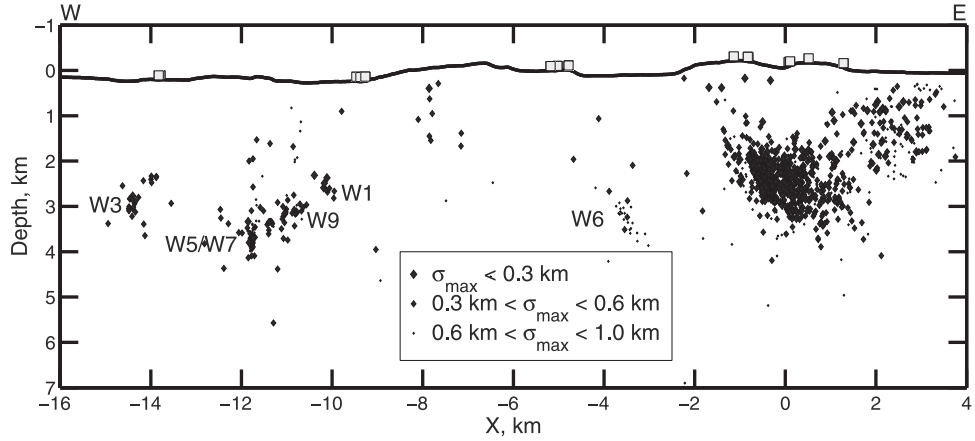

Figure 8. Projections of microearthquake hypocenters determined by HYPOINVERSE [*Klein*, 1978] (black diamonds) and stations (gray squares) onto a vertical plane oriented perpendicular to the ridge axis (Figure 2). Hypocenters are only shown for earthquakes with well-resolved depths, and the symbol sizes are scaled inversely with the maximum 1σ location uncertainty. Labels refer to the swarms listed in Table 2.

4.1. Earthquakes on the Western Flank

[32] The waveforms for earthquake swarms on the western flank are very coherent and thus particularly amenable to cross-correlation alignment. Figures 10a and 10b show example waveforms for these swarms aligned on the *S* arrival. Records for many of the off-axis instruments show secondary phases arriving either ~0.4 s after the *P* wave (Figure 10a) or ~0.4 s before the *S* wave (Figure 10b). We interpret these as *P-SV* and *SV-P* conversions at the base of layer 2A. Estimates of average layer 2A thickness on the Endeavour are 0.4 km from refraction data [*Cudrack and Clowes*, 1993] and 0.65 km from reflection data [*Rohr et al.*, 1988; *Rohr*, 1994]. Assuming $V_P = 2.65$ km s^{-1} in layer 2A [*Cudrack and Clowes*, 1993], a differential layer 2A travel time of 0.4 s requires $V_S = 0.7–1.0$ km s^{-1} (equivalent to a Poisson's ratio of 0.42–0.46). These values are compatible with observation on the East Pacific Rise [*Collier and Singh*, 1998] and Mid-Atlantic Ridge [*Barclay et al.*, 2001]. They are also quite consistent with the mean *S* wave station correction of −0.14 s (Table 1) which requires $V_S = 1.0–1.1$ km s^{-1} in layer 2A if the full correction is assigned to an increase in V_P/V_S in this layer.

[33] The only earthquake cluster on the western flanks within the network is located at midcrustal depths 12-km off axis. A relative relocation (Figure 11) shows that it actually comprises two distinct swarms; a small swarm (W5) on 7 July and a larger one (W7) slightly to the south and deeper starting on 13 June and continuing on 17 July. The swarms define two planes striking at ~35°, dipping steeply to the west, and separated vertically by 0.3 km. The faulted area for swarm W5 extends ~0.3 km along strike and 0.15 km vertically. For swarm W7, the faulted region measures ~0.4 km by 0.2 km. The earthquakes on 13 June occurred near the southern end of the cluster, the first 10 relocated earthquakes on 17 July migrated to the north and were followed by earthquakes throughout the faulted area. We were able to use *P* wave first motions and *P/S* amplitude ratios to determine double-couple focal mechanisms for seven earthquakes in swarm W7. They are all primarily strike-slip with east-west extension. One focal plane is consistent with the plane defined by the hypocenters.

[34] It is conceivable that timing errors, in particular nonlinear clock drift, could lead to systematic scatter in the relocated hypocenters. For this and other swarms, timing errors of ~0.1 s would be required to explain the observed cluster vectors. Since the maximum clock drift is only 1.5 ms d^{-1}, timing errors are unlikely to be of sufficient magnitude to produce the observed scatter. This inference is confirmed by examining differential *S* minus *P* times. For example, Figure 10a shows waveforms for OBS 59 for swarms W5 and W7; the differential *S-P* times vary by up to 0.04 s.

[35] Several other flank swarms to the north of the network are sufficiently close to permit relative relocations with free focal depths. A 4-day swarm (W1) with 55 relocated

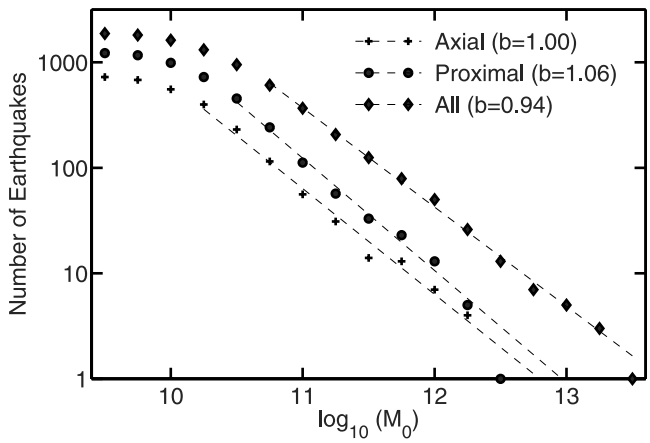

Figure 9. Cumulative number of earthquakes with a moment in excess of M_0 calculated for all located earthquakes (diamonds), proximal earthquakes within 3 km of the nearest OBS (crosses), and axial earthquakes within 1.5 km of the ridge axis and 3 km of the nearest OBS. At higher moments, least squares straight-line fits to the data yield *b* values close to 1.

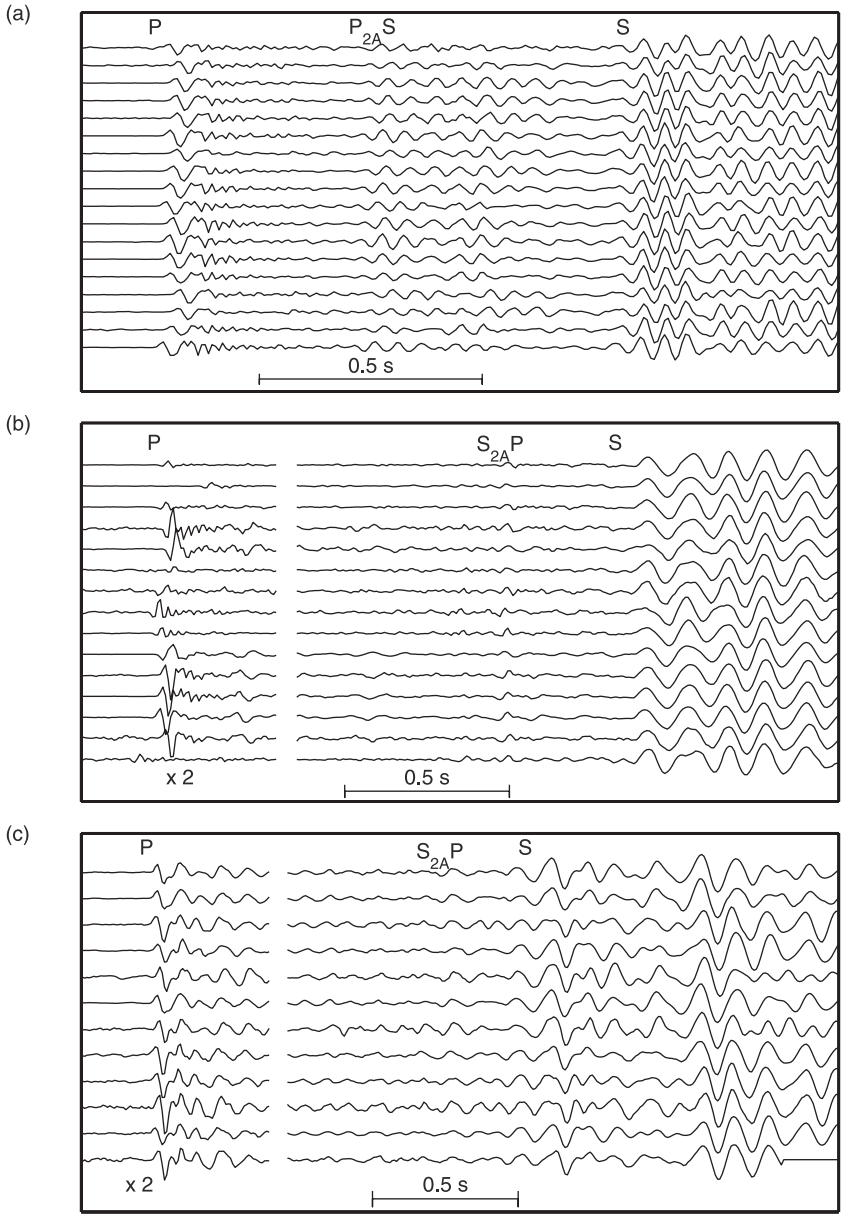

Figure 10. (a) Examples of waveforms recorded on the vertical channel of OBS 59 for swarms W5 and W7 (Figure 11). The *S* waveforms have been aligned by cross correlation, and the waveforms are normalized to equal maximum amplitude. The *P* waveforms are misaligned because of variation in the earthquake locations. A secondary arrival at a constant delay of just over 0.4 s relative to the *P* arrival is interpreted as a *P* to *SV* conversion at the base of layer 2A. (b) As for Figure 10a except the waveforms are recorded on OBS 63 for swarm W1 (Figure 12). For display purposes the amplitudes of the *P* waves have been magnified by a factor of 2. The *P* wave polarities and *P* to *S* amplitude ratios are variable as a result of variations in the focal mechanisms. A weak phase 0.4 s before the *S* wave is interpreted as an *SV* to *P* conversion at the base of layer 2A. (c) As for Figure 10b except the waveforms are for swarm A6 on the ridge axis.

earthquakes starting on 10 June (Figure 12) is located 11-km off axis and has the highest moment release of any swarm recorded near the network (Table 2). The epicenters extend ~1.5 km along a trend of ~35°. The cluster vector uncertainties are too large to determine a fault plane unambiguously, but they are most consistent with a fault plane dipping steeply to the west. However, the earthquakes may not fall on a single fault plane because the focal mechanisms are very variable. This is apparent from inspection of *P* wave polarities and *P/S* amplitude ratios in the seismograms (Figure 10b). Most of the mechanisms are strike-slip or extensional with east-west tension axes. The temporal distribution of hypocenters is complex but is not random (i.e., successive earthquakes tend to be located close to one another). Swarm W9 (Figure 12) on 25 July is located just to the southwest of swarm W1. The epicenters also appear to

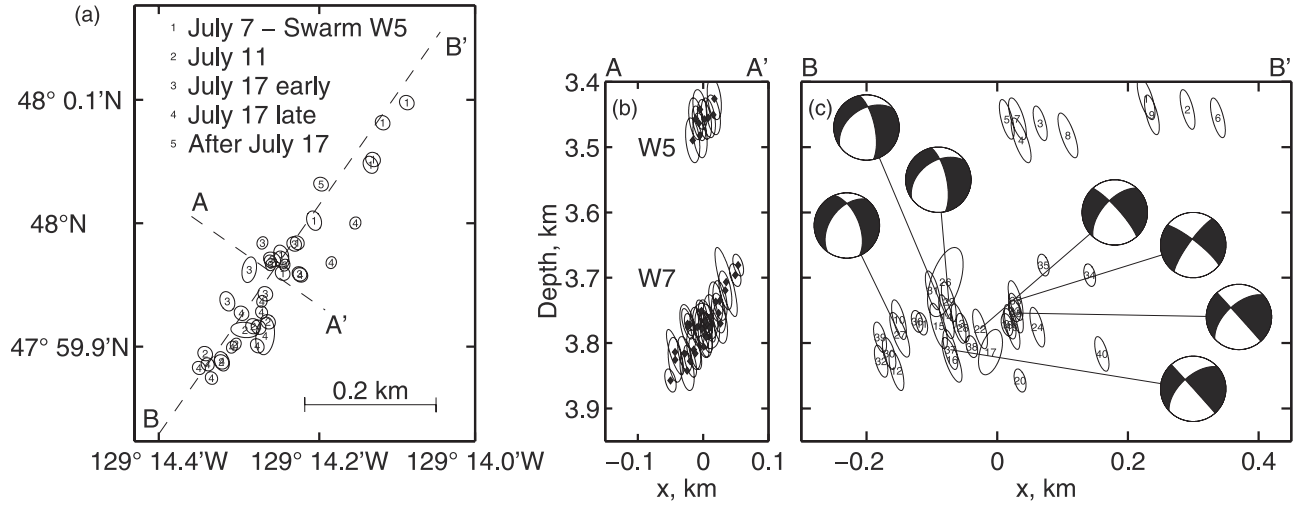

Figure 11. Results of a relative relocation for an earthquake swarms W5 and W7 (labeled in Figures 2 and 6). (a) Epicenters (numbers) and the projections of 50% confidence ellipsoids (solid lines) for the relative locations. The numbers indicate timing as described in the key. (b) Vertical profile oriented at 125°N. (c) Vertical profile oriented at 35°N. The numbers show the sequence of the earthquakes. Fault plane solutions are shown for seven events.

strike at ~45°, but they are too tightly grouped to resolve a fault plane. A composite focal mechanism is primarily strike-slip with an east-west tension axis.

[36] Swarm W3 (Figure 13) is located 14 km off axis, and the epicenters trend to the northeast at ~50° and are consistent with a steep fault plane. The swarm started on 18 June and lasted for 7 days. Midway through the swarm the center of activity migrated ~0.3 km to the northeast. A composite focal mechanism is nearly pure strike slip with north-south compression.

[37] On 12 July, swarm W6 (Figure 14) occurred ~3 km off axis near OBS 58, but because of triggering problems

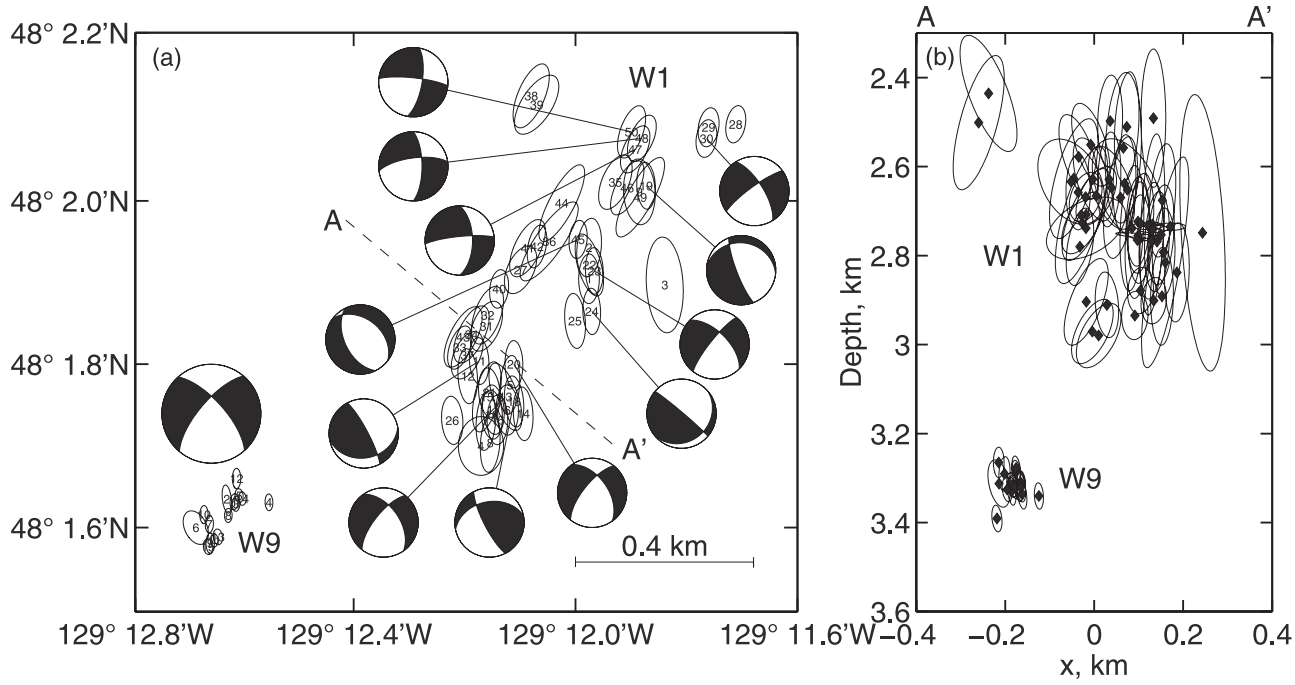

Figure 12. Results of relative relocations for swarms W1 and W9 plotted with the same conventions as Figure 12 in (a) map view and (b) projected onto a vertical cross section oriented at 130°. Because the waveforms are quite distinct, the two swarms have been relocated separately. Numbers in the map view show the sequence of events in the two swarms. The fault plane solutions for swarm W1 are very variable and are shown for individual events. The solution for the swarm W9 is a composite solution for 10 events.

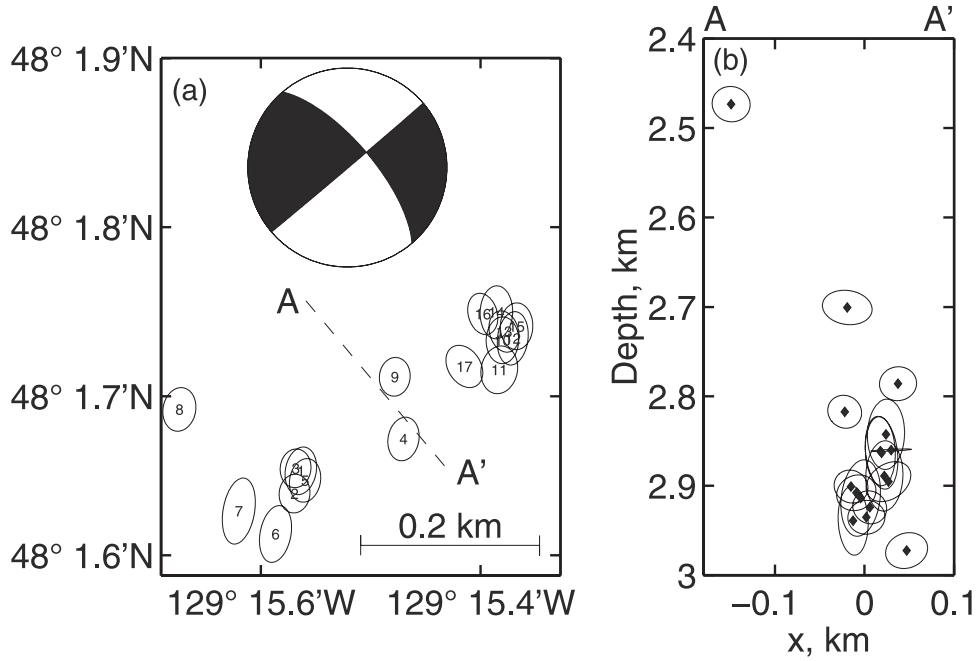

Figure 13. Results of a relative relocation for swarm W3 plotted with the same convention as Figure 12 in (a) map view and (b) projected onto a vertical cross-section oriented at 140°. The fault plane solution is a composite solution for 14 events.

this instrument recorded only four records for this swarm. The cluster vector uncertainties are fairly high and appear inconsistent with a single fault plane. The *P* wave polarities and *P/S* amplitude ratios require two distinct focal mechanisms: normal faulting with northwest-southeast extension for three earthquakes and strike slip with east-west extension for the rest.

[38] Three other swarms on the western flank (W2, W4, and W8) are too far from the network to relocate with an unconstrained focal depth or to determine focal mechanisms. Swarms W2 and W8 are the most westerly swarms and are located ~18 km off axis. Of the three swarms, only the cluster vector of swarm W8 is compatible with a point source.

[39] Figure 15a shows pressure and tension axes for 59 fault plane solutions for earthquakes located west of the ridge axis. The data set is dominated by earthquakes from the swarms of Figures 11–14, but also includes seven solutions for nonswarm earthquakes. The tension axes are consistently oriented perpendicular to the ridge axes and are primarily subhorizontal. The pressure axes show slightly more scatter but are dominated by north-south compression.

4.2. Axial Earthquakes

[40] Figure 16 shows origin times for axial earthquakes plotted as a function of along-axis coordinate. During the experiment, axial seismicity included a number of swarms (Table 2) and high levels of more uniformly distributed seismicity extending ~6 km along axis. The two largest axial swarms (A4 and A5) occurred on 27 June and 30 June and are located between High Rise and Salty Dawg vent fields. They include 78 and 101 located earthquakes, respectively. The cumulative moment releases are 0.7×10^{13} and 1.6×10^{13} N m, and together these swarms account for half of the moment release observed in the axial region. After these swarms, there was relatively little seismicity between the High Rise and Salty Dawg fields.

[41] We were able to relocate about two thirds of the events in swarms A4 and A5 using cross-correlated arrival times (Figure 17). The results show that the division into two swarms is somewhat arbitrary; the hypocenters for the two swarms overlap and define a planar feature that extends nearly 2 km along axis and dips at over 70° to the east. The

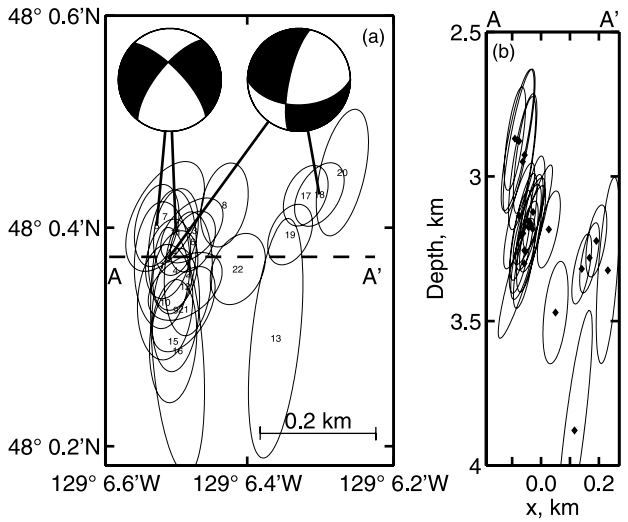

Figure 14. Results of a relative relocation for swarm W6 plotted with the same conventions as Figure 11 in (a) map view and (b) projected onto a vertical cross section oriented at 90°. Two distinct composite fault plane solutions have been derived from 3 and 12 events.

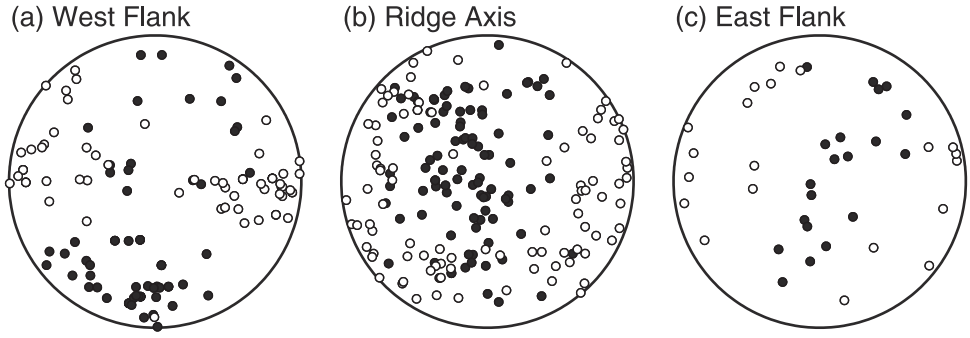

Figure 15. (a) Tension (open circles) and pressure axes (solid circles) for 59 fault plane solutions for individual earthquakes located west of the ridge axis, (b) 94 earthquakes located within 1.5 km of the ridge axis, and (c) 20 earthquakes located east of the ridge axis.

hypocenters show clear temporal patterns. For swarm A4 the first earthquakes were located at the lower north end of the swarm and over 3 days the seismically active area expanded steadily 0.8 km to the south. Swarm A5 lasted 17 hours and nearly half the earthquakes occurred in the first hour. During the first 30 min the hypocenters migrated 0.8 km southward along a linear trend that plunged southward from 2.4 to 2.7 km depth. During the next 30 min the seismicity migrated to shallower depths. About an hour after onset, small groups of earthquakes occurred at both ends of the initial trend. For the remainder of the swarm the seismicity was concentrated at the northern end and the active region expanded to greater depths.

[42] We identify five smaller axial swarms in Figure 16, all of which have a cumulative seismic moment an order of magnitude smaller than swarms A4 and A5. Waveform cross correlation was less successful for these swarms and as a result only ~40% of the events could be relocated. The relative location uncertainties are high but are adequate to show that all swarms except A6 are inconsistent with a point source. There are three reasons for the poor cross correlations. First, smaller earthquakes have lower signal to noise. Second, the *S* waves for these events are often emergent, and many alignments had to be discarded because of cycle ambiguities. Finally, it appears that the shapes of waveforms vary more rapidly with earthquake locations to the south of High Rise vent field, perhaps as a result of complexities in the velocity structure. Although we have not quantified the effect, the relative amplitude of *P* wave coda seems to be larger for earthquakes in this region (e.g., Figure 10c) suggesting that there is more scattered energy.

[43] To relocate all the axial earthquakes with sufficient cross-correlated picks, we divided them into overlapping subsets that extend 1 km along axis and are spaced 0.5 km apart. We relocated the subsets using the method of *Jordan and Sverdrup* [1981] and used the new locations to reassign earthquakes to subsets. This process was repeated until the subsets converged. We then adjusted the hypocentroids for each subset to minimize the offset between hypocenters for earthquakes that are common to two subsets. After these adjustments the alternative hypocenters generally fall within each other's 50% confidence limits. To combine the subsets, we selected the hypocenter that lay closest to its hypocentroid.

[44] We were able to relocate 325 of 676 axial earthquakes, and the results are shown in Figures 18 and 19. Inspection of Figure 18a shows that the relocation tends to exclude earthquakes with outlying epicenters. Similarly, it generally excludes earthquakes at the depth extremes. Many outliers are small poorly recorded events that may be mislocated. However, others are well recorded, and the hypocentral uncertainties obtained by HYPOINVERSE suggest that they do not lie within the tight clusters defined by the relocation. Indeed, the very absence of good waveform cross correlations for these earthquakes suggests that their locations are scattered.

[45] The relocated epicenters shows that the steeply dipping plane of seismicity defined by swarms A4 and A5 (Figures 19a and 19b) merges at its base to the south with a seismically active volume measuring ~1 km in all directions beneath High Rise vent field (Figures 19c and 19d). Several additional planar features are apparent in the cross sections of Figures 19b–19d but the hypocentral uncertainties are sufficient only to show that the locations are inconsistent with a single fault plane. Although there are quite a few earthquakes farther to the south, we were only able to relocate two small clusters at ~3 km depth beneath Main and Mothra vent field (Figures 19e and 19f).

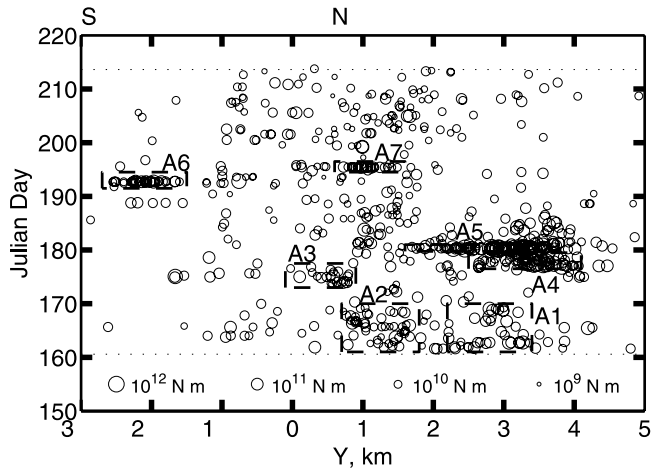

Figure 16. Time of axial earthquakes as a function of position along axis (determined by HYPOINVERSE [*Klein*, 1978]) relative to the Main vent field. The symbol size is scaled to the logarithm of the earthquake moment. Dotted lines show the start and end times of the experiment, and labeled dashed boxes enclose events in swarms A1–A7.

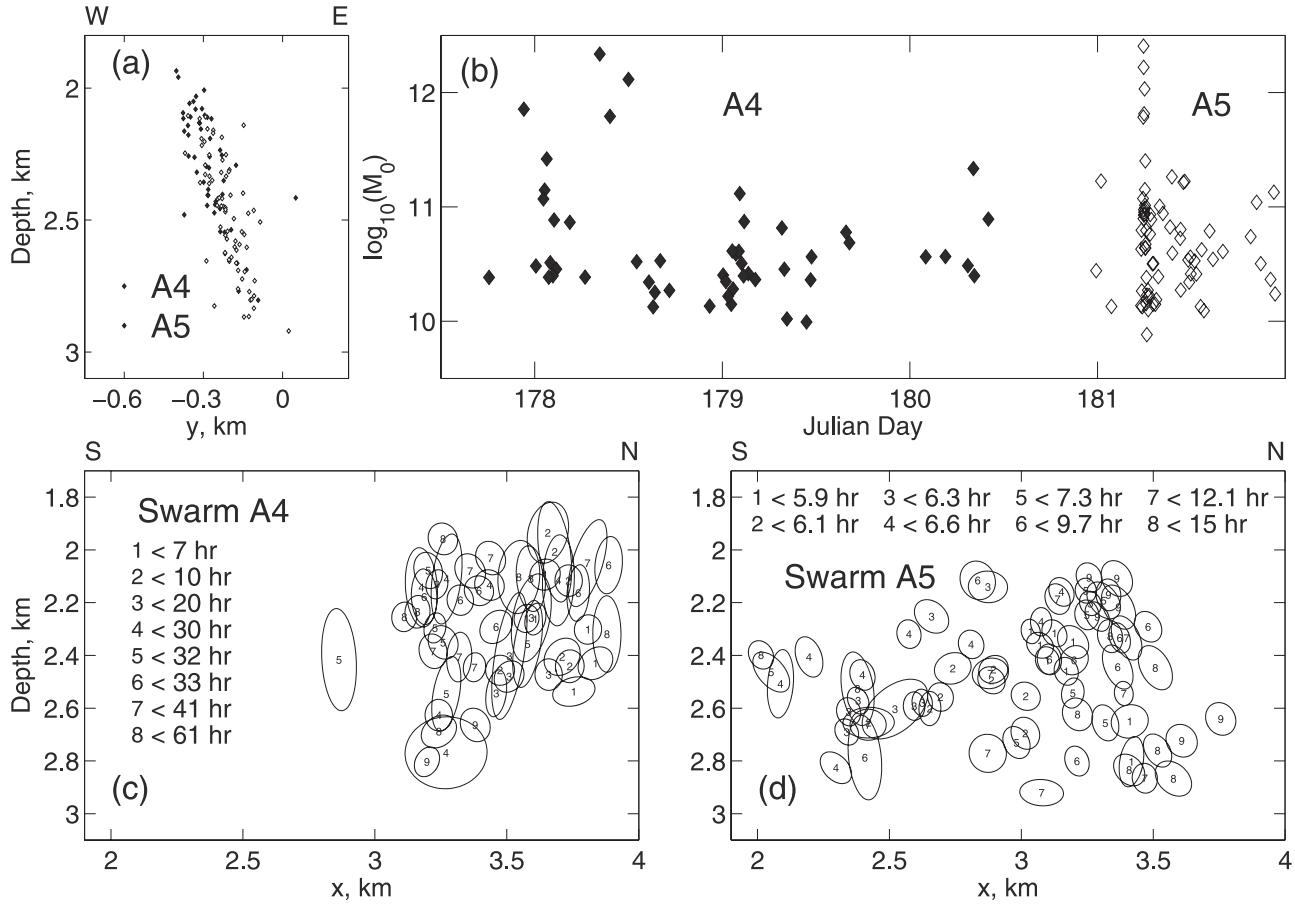

Figure 17. Relative event locations for axial swarms A4 and A5. (a) Cross section oriented perpendicular to the ridge axis (110°N) showing hypocenters for swarms A4 (solid diamonds) and A5 (open diamonds). (b) Moments versus origin times for earthquakes in these swarms. (c) Cross section oriented parallel to the ridge axis (020°N) showing hypocenters (numbers) and 50% confidence ellipsoids for swarm A4. The numbers indicate relative timing and the times in the key are relative to the first event. (d) As for Figure 17c except for swarm A5.

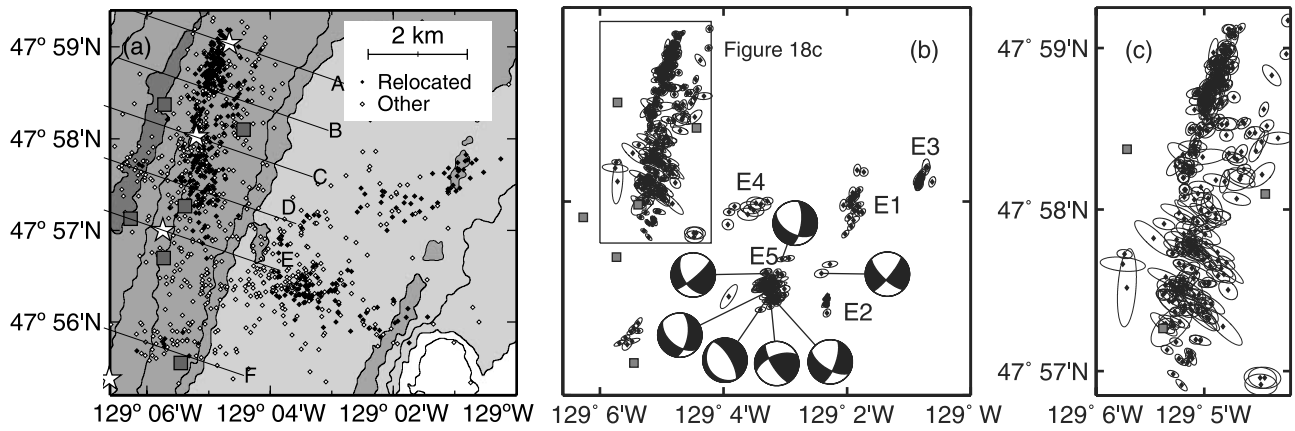

Figure 18. (a) SeaBeam bathymetric map (contoured at 100-m intervals with depths shaded as in Figure 1) showing the location of ocean bottom seismometers (gray squares), four high temperature vent fields (stars), and epicenters (diamonds) determined with HYPOINVERSE [*Klein*, 1978] for earthquakes on axis and to the east of the ridge axis. Solid diamonds indicate events that have been successfully relocated using the cross-correlation relative relocation technique. Solid lines labeled A–F show the location of cross sections shown in Figure 19. (b) Epicenters (diamonds) and the projections of 50% confidence ellipsoids for relative relocation. Examples of fault plane solutions are also show for off-axis earthquakes. (c) Relocated epicenters and 50% confidence limits for the northern axial region outlined by the box in Figure 18b.

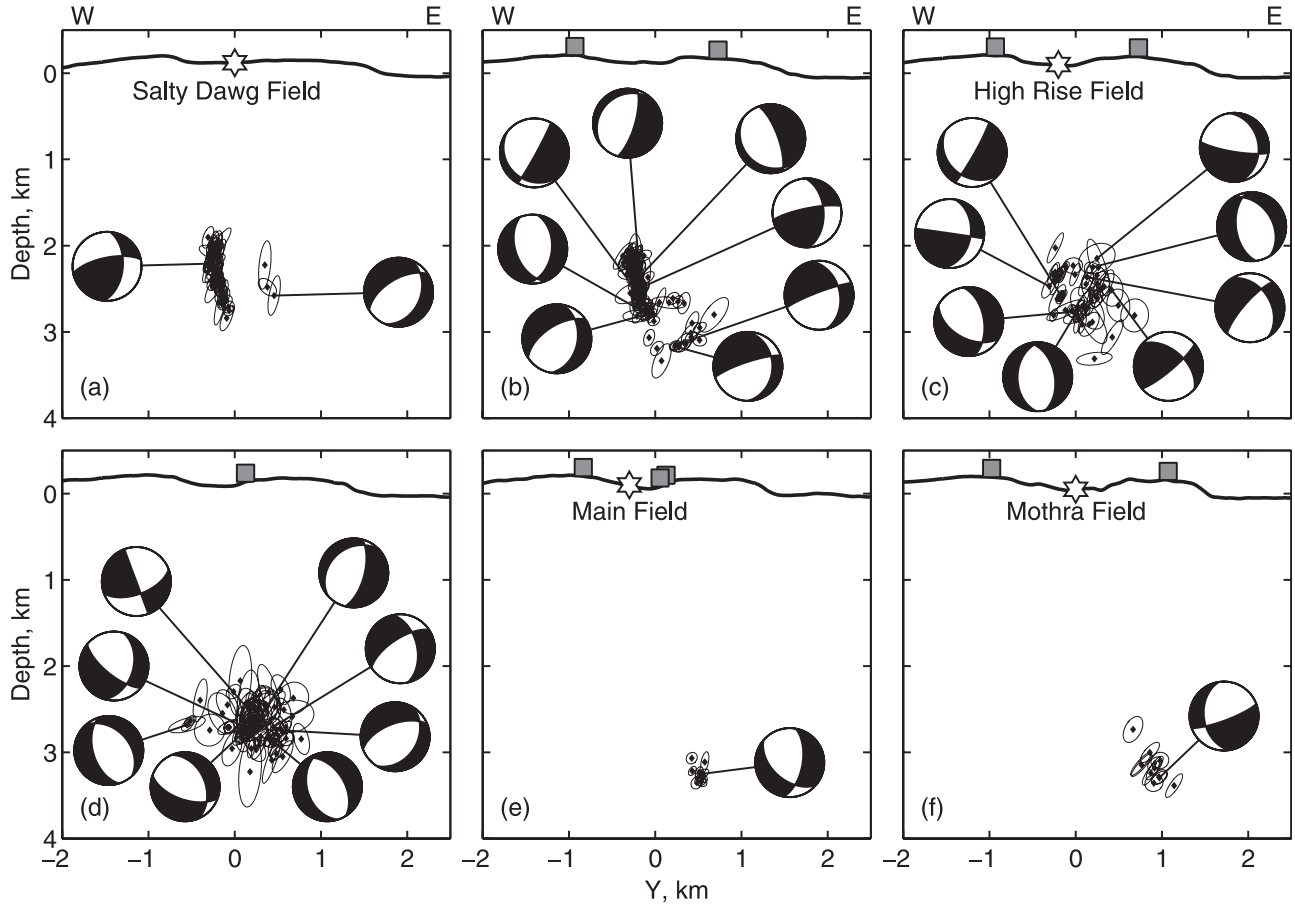

Figure 19. Relative locations of axial events (diamonds) and 50% confidence ellipsoids (solid) projected onto six vertical cross sections oriented perpendicular to the ridge axis. The section locations are shown in Figure 18; sections in Figures 19a–19e are spaced 1 km apart, while Figure 19f is located 2.25 km to the south of Figure 19e. Hypocenters are projected a maximum distance of 0.5 km. The plots also show examples of fault plane solutions determined for individual events.

[46] We determined double-couple focal mechanisms for 94 earthquakes; examples are shown in Figure 19. The mechanisms are dominated by normal faulting and often include a strike-slip component. The tension axes (Figure 15c) are mostly subhorizontal. The average orientation is approximately perpendicular to the ridge axis, but they show a lot of scatter. We identified only two earthquakes whose mechanisms are clearly not double couple. Both appear to have compressional first motions in all directions.

4.3. Earthquakes on the Eastern Flank

[47] Because there were no OBSs deployed on the eastern flank, the hypocenters in this region have relatively large uncertainties. The most prominent feature of the HYPOINVERSE epicenters (Figures 2 and 18a) is a diffuse band of ~250 earthquakes striking perpendicular to the ridge axis at ~110° from the Main vent field and extending ~5 km off axis. This band coincides approximately with a relic transfer zone (Figure 1) which formerly connected a failed propagator on the Cobb segment to the Endeavour [*Johnson et al.*, 1983]. Well-constrained focal depths are generally <2 km (Figure 8). Several smaller clusters farther to the north appear to define a second diffuse band striking at ~75°.

[48] Relative relocations clearly show that the bands are artifacts of hypocentral errors, at least at their eastern ends (Figure 18b). The more distant earthquakes in the first band relocate into two swarms. Swarm E2 is a short swarm on 8 July comprising over 30 earthquakes. The swarm is located 5 km off axis and the cluster vector errors are consistent with a point source. Swarm E5 includes over 100 earthquakes and is located 3 km off axis. This swarm includes earthquakes throughout the experiment but most occur after 24 July. The cluster vector has large uncertainties but the relocated epicenters are not consistent with a point source. The earthquakes at the eastern end of the second band also belong to two swarms. Swarm E1 is located 4 km off axis, and the relocated epicenters align along a strike of ~10°. Swarm E3 is located 5 km off axis, and the cluster vector is consistent with a point source.

[49] Nearer the ridge axis, relocated epicenters for a swarm E4 appear to be aligned at ~60°. However, the *S* waveform alignments for this swarm are not very robust. There is also a significant number of earthquakes between the Main vent field and 129° 4′W (~2 km off axis) that have not been successfully relocated (Figure 18a). These earthquakes are typically quite small ($M_0 < 3 \times 10^{10}$ N m),

and the more westerly epicenters may be part of swarm E5. The remainder are distributed fairly uniformly in time and their waveforms, particularly the *S* waves recorded on OBSs 50 and 52, are very varied. We infer that the locations are probably scattered.

[50] Figure 15c shows focal mechanisms for 20 earthquakes mostly from the swarm of 24 July. Because of the poorer network geometry in this region we have included mechanisms that are less robust than those shown for western flank and axial events. The focal mechanisms are primarily extensional with some strike slip. The tension axes tend to be oriented subperpendicular to the ridge axis.

5. Discussion

[51] Fifty-five days is a short interval in which to characterize long-term patterns of seismicity. On the Endeavour, there are sufficient observations from regional land networks, a decade of *T* phase monitoring [*Dziak and Fox*, 1995; *Johnson et al.*, 2000] and previous OBS deployments [*McClain et al.*, 1993] to show that the high levels of seismicity recorded during our experiment are not atypical. While our results may not be fully representative of the distribution of earthquakes over the longer term, they do provide insights into the nature of earthquake swarms in young oceanic crust, the effect of ongoing plate reorganization in the region, and the subsurface configuration of axial hydrothermal circulation. We discuss each of these topics in turn.

5.1. Earthquake Swarms

[52] Teleseismic [*Bergman and Solomon*, 1990] and microearthquake studies [*Toomey et al.*, 1985, 1988; *Kong et al.*, 1992; *Wolfe et al.*, 1995; *Barclay et al.*, 2001] on slow spreading ridges show that many tectonic earthquakes occur in swarms. On faster spreading ridges, swarms beneath hydrothermal vent fields can dominate the earthquake count [*Sohn et al.*, 1998a]. Over half the located earthquakes in our experiment belong to the 25 swarms listed in Table 2. The moments of swarm earthquakes show no consistent temporal patterns. Most swarms lasted from 1 hour to over a week, although a few include earthquakes scattered throughout the experiment.

[53] Our relative relocations show that most swarms are not compatible with a point source. Earthquakes are typically distributed over regions with dimensions ranging from a few hundred meters up to about a kilometer. The hypocenters for swarms within or near the network are generally compatible with a single fault plane. The earthquake locations often show temporal patterns. These can be quite complex, but in some instances, earthquakes migrate systematically from one end of the swarm to the other at velocities that appear to range from $\sim$100 m d^{-1} to $\sim$1 km h^{-1}. Because we can only identify clear corner frequencies for larger earthquakes, we cannot determine the fault radii of smaller events. If we assume that the average stress drop determined for larger earthquakes ($\sim$1 MPa) is independent of seismic moment, we can infer that most swarms do not rupture the whole fault plane.

[54] These swarm characteristics are very similar to those observed in a variety of settings on land [e.g., *Deichmann and Garcia-Fernandez*, 1992; *Slunga et al.*, 1995; *Shearer*, 1998]. Two principal mechanisms have been advanced to explain nonforeshock/aftershock earthquake swarm sequences [*Deichmann and Garcia-Fernandez*, 1992]; propagating failure due to cascading changes in static stress and failure due to fluctuations in pore pressure along the fault plane. At Parkfield, *Johnson and McEvilly* [1995] argue that the occurrence of periodic nearly identical microearthquakes (multiplets) that repeatedly rupture the same fault patch is most simply explained by models in which failure is driven by fluctuations in fluid pressures. They argue that the observation that earthquake swarms often diffuse outward from the initial event suggests that failure occurs when fluid is expelled from overpressured fault patches.

[55] Our observations cannot discriminate between the alternate mechanisms. The temporal distribution of hypocenters is clearly more complex than an idealized model based on the diffusion of overpressured pore fluids [*Johnson and McEvilly*, 1995]. This could be partially an artifact of relatively high relocation errors and could also reflect heterogeneous fault zone permeability. If fluid pressure variations are involved, our results have interesting implications for the hydrology of young oceanic crust. All the well-located swarms are at depths of 2–4 km. If these regions are commonly overpressured, it can be inferred that hydrothermal circulation at purely hydrostatic pressures is limited to the upper 2 km along many fault segments.

5.2. Effects of Regional Tectonics

[56] As noted in section 1, the high levels of seismicity on the Endeavour could be a result either of the normal cyclical processes on intermediate spreading ridges or a manifestation of the complex tectonics of the region. Studies on the fast spreading East Pacific Rise have shown that the normal faults can remain active up to 30 km off axis [*Lee and Solomon*, 1995; *Alexander and Macdonald*, 1996]. On the western flank of the Endeavour, submersible observations provide evidence for recent slip on normal faults up to 12 km off axis [*Johnson et al.*, 1993]. Our study confirms that the western flank is seismically active, but neither the hypocenters nor the focal mechanism are generally compatible with simple ridge-perpendicular extension.

[57] The hypocenters for four well-located swarms (W1, W3, W5, and W7) are consistent with steeply dipping fault planes striking between 035° and 050°N. None of the swarms on the western flank are consistent with faults striking at 020°N, the orientation of the ridge axis and abyssal hills. Errors in the velocity structure could distort relocated hypocenters if the predicted ray takeoff directions are systematically wrong. Errors of 15–30° in apparent strike would require a strongly heterogeneous velocity structure, which seems unlikely on the ridge flanks. The focal mechanisms are fit well by double-couple mechanisms and thus show no evidence for large errors in takeoff angles. While the tension axes are generally oriented perpendicular to the ridge axis, the majority of focal mechanism solutions are strike slip with north-south pressure axes. We infer that the swarms on the western flank are influenced by regional tectonics.

[58] In June 1999, the SOSUS network recorded a swarm of over 2500 earthquakes [*Johnson et al.*, 2000] including a magnitude $M_L = 4$ earthquake on 9 June and several others that were large enough to be recorded on land. *T* phase

epicenters scatter over a 30 × 30 km area, and formal location errors for individual epicenters are quite large (~10 km at the 95% confidence level) [*Johnson et al.*, 2000]. Most earthquakes are located on the western flank with a mean location well to the south of our experiment, but the largest shock was located near the center of our network. A moment tensor solution determined by modeling body waves recorded on land [*Nabelek and Ganyuan*, 1995] is a normal faulting mechanism with focal planes striking at ~315°N [*Johnson et al.*, 2000]. It is neither compatible with ridge-perpendicular extension nor with the mechanisms we report for the western flank. It provides additional evidence for the anomalous nature of the seismicity on the Endeavour, but given the large epicentral uncertainties, it is difficult to interpret further.

[59] The north-south compression inferred from our focal mechanisms is consistent with regional tectonics. Earthquake pressure axes tend to be aligned approximately north-south in the Pacific Northwest because the Juan de Fuca plate is compressed by the northward motion of the Pacific plate relative to North America. It is well established that compressive forces transmitted across the Mendocino transform drive the deformation of the Gorda plate [*Wang et al.*, 1997], and the uplift of rotated blocks in the Sovanco transform zone [*Cowan et al.*, 1986] may be evidence of north-south crustal shortening across this transform. Earthquake focal mechanisms on the Explorer plate are very similar to those we report on the western flank; they are predominately strike-slip with north-south compression. *Rohr and Furlong* [1995] argue that the Explorer plate is being split in two as the Queen Charlotte transform fault extends southward to meet the Juan de Fuca Ridge and Nootka fault zones. In this model the northeast and southwest portions of the Explorer will attach to the North American and Pacific plates, respectively, as motions on the Explorer subduction tone, Sovanco transform, and Explorer Ridge cease. The current configuration of the Explorer plate is controversial, but *Kreemer et al.* [1998] estimate the strain field from a catalog of earthquakes and argue that the Explorer transform zone has already formed.

[60] The reorganization of the Explorer plate has been ongoing for the past ~5 Myr, which is a much longer period than the maximum crustal age of ~0.5 Myr within our network. If the north-south compression arises from the deformation of the Explorer plate, it may at first seem surprising that it has not modified the morphology of the ridge-parallel abyssal hills. However, there is plenty of evidence to suggest that configuration of the Endeavour has evolved over a much shorter timescale. To the north, the Endeavour offset formed ~0.2 Myr ago when spreading jumped from Middle Valley to West Valley [*Davis and Lister*, 1977; *Karsten et al.*, 1986]. To the south, the Cobb offset has undergone net northward propagation over the past few million years, punctuated by short episodes of reversed motion [*Johnson et al.*, 1983]. The latest episode of northward propagation commenced only 0.05 Myr ago [*Delaney et al.*, 1981], and current migration rate is 0.4–0.9 m yr^{-1} [*Shoberg et al.*, 1991]. *Karsten et al.* [1990] have suggested that much, if not all, of the Endeavour rift is in the process of failing.

[61] In this context, the focal mechanisms that we observe on the west flank can be interpreted in two ways. If the Explorer ridge has now extended to the south, as it apparently did once before in the past 1–2 Myr [*Wilson*, 1993], the west flank of the Endeavour may now be part of the Sovanco deformation zone. Alternatively, if an incipient Explorer transform has split the Explorer plate in two [*Rohr and Furlong*, 1995; *Kreemer et al.*, 1998], its southern end may be evolving to intersect the Juan de Fuca Ridge near our experiment site and well to the south of the current JdFR-Sovanco-Nootka triple junction.

5.3. Axial Seismicity and Hydrothermal Circulation

[62] Nearly all of the axial earthquakes are located at depths of 1.5–3.5 km, and there is no significant seismicity below 4 km. The lack of earthquakes at shallower depths both here and off axis is consistent with faulting models that predict stable sliding at low confining pressures [*Scholz*, 1988; *Cowie et al.*, 1993]. The maximum depth can be interpreted in terms of the thermal structure. Brittle deformation will cease once temperatures exceed ~600° [*Cowie et al.*, 1993]. The average crustal age beneath the axial valley (10,000 years) corresponds to a conductive length scale of only ~500 m. Thus we can infer that hydrothermal fluids have circulated and cooled the crust to depths approaching the maximum depth of seismicity.

[63] There are nearly 100 well-resolved focal mechanisms for axial earthquakes, and they are quite varied. They are characterized by subhorizontal tension axes that are distributed relatively uniformly at all azimuths except parallel to the ridge axis. One interpretation of this pattern is that it reflects the combined and roughly equally weighted effects of tension perpendicular to the ridge axis due to spreading and tension in all horizontal directions due to hydrothermal cooling. The horizontal strain rate from cooling at any point is

$$\dot{\varepsilon}_{Hy} = \frac{dT}{dt}\alpha_l, \tag{4}$$

where dT/dt is the rate of cooling and α_l is the linear coefficient of thermal expansion. For a volume being cooled uniformly by hydrothermal circulation, this can be expressed

$$\dot{\varepsilon}_{Hy} = \frac{Q\alpha_l}{V\rho c_p}, \tag{5}$$

where Q is the hydrothermal heat flux, V is the volume of crust being cooled, ρ is the density of the crust, c_p is its specific heat capacity, and α_l is the linear coefficient of thermal expansion. There have been numerous attempts to quantify the hydrothermal heat flux from the Main vent field and from the central portion of the Endeavour segment [*Rosenberg et al.*, 1988; *Baker and Hammond*, 1992; *Schultz et al.*, 1992; *Thomson et al.*, 1992; *Bemis et al.*, 1993; *Ginster et al.*, 1994; *Stahr et al.*, 2000]. Estimates vary from 10^2 to 10^4 MW, although the most accurate measurement for the Main field is 600 ± 100 MW [*Stahr et al.*, 2000]. From the distribution of axial earthquakes, the cross-sectional area of seismically active region is ~1 km^2 and so for vent fields spaced 2-km apart, $V \approx 2$ km^3. Taking $\alpha_l = 6 \times 10^{-6}$ K^{-1}, $\rho = 2800$ kg m^{-3}, and $c_p = 10^3$ J kg^{-1} K^{-1} yields $\dot{\varepsilon}_{Hy} = 10^{-13}$–$10^{-11}$ s^{-1}. If plate boundary

extension is distributed over a 1-km-wide region, the tectonic strain rate is 2×10^{-12} s^{-1}, which lies near the middle of the range estimated for hydrothermal cooling.

[64] One puzzling feature of the axial seismic structure is the axial reflector imaged by *Rohr et al.* [1988]. Although this feature looks like AMC reflectors imaged elsewhere, *Rohr et al.* [1988] are cautious not to interpret it as such because the signal to noise is too low to determine the polarity. Tomographic inversions [*White and Clowes*, 1990] show no evidence of a crustal magma chamber at 1.5–3.5 km depth, although the data would not resolve a small magma chamber and the surrounding thermal anomaly if it measured less than ~1 km × 1 km. Above the reflector, inversions do resolve a region of low velocities and high attenuation at 1–2 km depth that is interpreted as a region of high porosity [*White and Clowes*, 1990, 1994].

[65] The reflection [*Rohr et al.*, 1988] and refraction tomography profiles [*White and Clowes*, 1990] cross the rise axis just to the north of our network near the profile of Figure 19a. Assuming the velocity model we used to locate earthquakes (Figure 3), the axial reflector [*Rohr et al.*, 1988] is located 2.3 km beneath the seafloor. Along this profile, the relocated earthquakes extend from ~2 to 3 km depth. Although the earthquakes are just outside the network, the depths are well resolved. Axial earthquakes may be systematically located too deep if V_P/V_S is higher on axis than the average value determined for our network. Conversely, depths may be underestimated because many *S* waves for axial earthquakes are emergent and we picked these ambiguous arrivals at the earliest plausible time. While it is difficult to state categorically the maximum possible bias to the earthquake depths, it is probable that the seismicity does extend below the axial reflector. Since most of the axial earthquakes to the north of the network lie on a steeply dipping plane beneath the west wall, our data do not preclude the existence of a small axial magma chamber located just to the east. Alternatively, the reflection could arise from a sharp decrease in porosity [*White and Clowes*, 1994], perhaps overlying a recently solidified magma chamber. Farther to the south where the hypocenters are more scattered, any axial magma body would most likely underlie the seismicity.

[66] Building on the interpretation of *McClain et al.* [1993], *Wilcock and Delaney* [1997] argue that hydrothermal circulation on the Endeavour is driven by the active penetration into hot crust rather than by circulation above a steady state magma chamber. In support of this argument they cite the relatively large size of sulfide structures, the absence of recent eruptions, the high hydrothermal heat flux, and the high levels of seismicity. The distribution of earthquakes and the focal mechanisms that we observed are consistent with this interpretation. While it would be overly simplistic to infer fluid pathways from 2 months of seismicity, the distributions of intense axial seismicity and hydrothermal cooling on this segment are likely to be closely related.

6. Conclusions

[67] We have presented the results of a 55-day microearthquake experiment on the Endeavour segment. Microearthquake activity was high throughout the experiment. Hypocenters have been determined for 1750 earthquakes using at least one *S* wave and five total arrival times. Focal mechanisms were obtained for 173 earthquakes using *P* wave first motions and *P/S* amplitude ratios. Seismic moments vary from 10^9 to 4×10^{13} N m and 70% of the total moment release of 3.5×10^{14} N m occurred in distant events. The primary conclusions of our study are as follows:

1. Over half the earthquakes occurred in 25 swarms located both on and off axis. Relative relocations of swarms near the network obtained with a waveform cross-correlation technique locate the swarms at 2–4 km depth and generally resolve clear but complex temporal patterns in the distribution of hypocenters. If swarms result from the diffusion of overpressured fluids as has been proposed elsewhere, then our results suggest that the fluids in many fault segments can exceed hydrostatic pressures below 2 km depth.

2. On the west flank, swarms were observed up to 18 km off axis in regions of ridge parallel abyssal hills. Neither the fault planes inferred from relative relocations nor the focal mechanisms are compatible with ridge-parallel extension. Rather the mechanisms are predominantly strike slip with north-south compression and are similar to those observed on the Explorer plate. We infer that seismicity on this flank is affected by the reorganization of the Explorer plate and speculate that the anomalous seismicity may be related to recent rift failure on the Endeavour.

3. Earthquakes beneath the axial valley define a region of intense seismicity at 1.5–3.5 km depth that appears to extend beneath the weak axial reflector imaged by *Rohr et al.* [1988]. Beneath Salty Dawg vent field the seismicity is dominated by two swarms beneath the west valley wall. These earthquakes define a plane striking parallel to the ridge axis and dipping at 70° to the east. Farther to the south the earthquakes are not compatible with a single plane. The focal mechanisms are characterized by subhorizontal tension axes oriented at all azimuths except ridge parallel and may reflect a stress regime that is equally influenced by ridge-perpendicular extension and hydrothermal cooling. These characteristics are compatible with models that suggest hydrothermal circulation on the Endeavour is actively mining heat from midcrustal depths.

[68] **Acknowledgments.** We thank John Bailey, Jim Dolan, David DuBois, John Hallinan, and Beecher Wooding for their technical expertise with the OBS instruments; the captain and crew of the R/V *Wecoma* for considerable assistance in carrying out the experiment; and two anonymous reviewers and an Associate Editor for comments on the manuscript. This work was supported by the National Science Foundation under grants OCE-9403668 and OCE-9403409.

References

Alexander, R. T., and K. C. Macdonald, Sea Beam, Sea MARC II and *Alvin*-based studies of faulting on the East Pacific Rise 9°20′N-9°50′N, *Mar. Geophys. Res.*, *18*, 557–587, 1996.

Almendros, J., A. H. Barclay, W. S. D. Wilcock, and G. M. Purdy, Seismic anisotropy of the shallow crust at the Juan de Fuca Ridge, *Geophys Res. Lett.*, *27*, 3109–3112, 1999.

Baker, E. T., and S. R. Hammond, Hydrothermal venting and the apparent magmatic budget of the Juan de Fuca Ridge, *J. Geophys. Res.*, *97*, 3443–3456, 1992.

Barclay, A. H., D. R. Toomey, and S. C. Solomon, Microearthquake characteristics and crustal V_P/V_S structure at the Mid-Atlantic Ridge, 35°N, *J. Geophys. Res.*, *106*, 2017–2034, 2001.

Bemis, K. G., R. P. Von Herzen, and M. J. Mottl, Geothermal heat flux from hydrothermal plumes on the Juan de Fuca Ridge, *J. Geophys. Res.*, *98*, 6351–6365, 1993.

Bergman, E. A., and S. C. Solomon, Earthquake swarms on the Mid-Atlantic Ridge: Products of magmatism or extensional tectonics?, *J. Geophys. Res.*, *95*, 4943–4965, 1990.

Brune, J. N., Tectonic stress and the spectra of seismic shear waves from earthquakes, *J. Geophys. Res.*, *75*, 4997–5009, 1970.

Collier, J. S., and S. C. Singh, Poisson's ratio structure of young oceanic crust, *J. Geophys. Res.*, *103*, 20,981–20,996, 1998.

Cowan, D. S., M. Botros, and H. P. Johnson, Bookshelf tectonics: Rotated crustal blocks within the Sovanco fracture zone, *Geophys. Res. Lett.*, *13*, 995–998, 1986.

Cowie, P. A., C. H. Scholz, M. Edwards, and A. Malinverno, Fault strain and seismic coupling on mid-ocean ridges, *J. Geophys. Res.*, *98*, 17,911–17,920, 1993.

Creager, K. C., and L. M. Dorman, Location of instruments on the seafloor by joint adjustment of instrument and ship and positions, *J. Geophys. Res.*, *87*, 8379–8388, 1982.

Cudrack, C. F., and R. M. Clowes, Crustal structure of the Endeavour ridge segment, Juan de Fuca Ridge, from a detailed seismic refraction study, *J. Geophys. Res.*, *98*, 6329–6349, 1993.

Davis, E. E., and C. R. B. Lister, Tectonic structures on the Juan de Fuca Ridge, *Geol Soc. Am. Bull.*, *88*, 346–363, 1977.

Deichmann, N., and M. Garcia-Fernandez, Rupture geometry from high-precision relative hypocenter locations of microearthquake clusters, *Geophys. J. Int.*, *110*, 501–517, 1992.

Delaney, J. R., H. P. Johnson, and J. L. Karsten, The Juan de Fuca Ridge-hotspot-propagating rift system: New tectonic, geochemical, and magnetic data, *J. Geophys. Res.*, *86*, 11,747–11,750, 1981.

Delaney, J. R., V. Robigou, R. E. McDuff, and M. K. Tivey, Geology of a vigorous hydrothermal system on the Endeavour segment, Juan de Fuca Ridge, *J. Geophys. Res.*, *97*, 19,663–19,682, 1992.

Dziak, R. P., and C. G. Fox, Juan de Fuca Ridge T-wave earthquakes August 1991 to present: Volcanic and tectonic implications (abstract), *Eos Trans. AGU*, *76*(46), Fall Meet. Suppl., F411, 1995.

Francis, T. J. G., The ratio of compressional to shear velocity and rock porosity on the axis of the Mid-Atlantic Ridge, *J. Geophys. Res.*, *81*, 4361–4364, 1976.

Ginster, U., M. J. Mottl, and R. P. Von Herzen, Heat flux from black smokers on the Endeavour and Cleft segments, Juan de Fuca Ridge, *J. Geophys. Res.*, *99*, 4937–4950, 1994.

Hooft, E. E. E., and R. S. Detrick, Relationship between axial morphology, crustal thickness, and mantle temperature along the Juan de Fuca and Gorda Ridges, *J. Geophys. Res.*, *100*, 22,499–22,508, 1995.

Hyndman, R. D., R. P. Riddihough, and R. Herzer, The Nootka fault zone - a new plate boundary off western Canada, *Geophys. J.R. Astron. Soc.*, *58*, 667–683, 1979.

Jacobson, R. S., L. M. Dorman, G. M. Purdy, A. Schultz, and S. C. Solomon, Ocean bottom seismometer facilities available, *Eos Trans. AGU*, *72*, 506, 515, 1991.

Johnson, H. P., J. L. Karsten, J. R. Delaney, E. E. Davis, R. G. Currie, and R. L. Chase, A detailed study of the Cobb Offset on the Juan de Fuca Ridge: Evolution of the propagating rift, *J. Geophys. Res.*, *88*, 2297–2315, 1983.

Johnson, H. P., K. Becker, and R. Von Herzen, Near-axis heat flow measurements on the northern Juan de Fuca Ridge: Implications for fluid circulation in oceanic crust, *Geophys. Res. Lett.*, *20*, 1875–1878, 1993.

Johnson, H. P., M. Hutnak, R. P. Dziak, C. G. Fox, I. Urcuyo, J. P. Cowen, J. Nabalek, and C. Fisher, Earthquake-induced changes in a hydrothermal system on the Juan de Fuca Ridge mid-ocean ridge, *Nature*, *407*, 174–177, 2000.

Johnson, P. A., and T. V. McEvilly, Parkfield seismicity: Fluid driven?, *J. Geophys. Res.*, *100*, 12,937–12,950, 1995.

Jordan, T. H., and K. A. Sverdrup, Teleseismic location techniques and their application to earthquake clusters in the south-central Pacific, *Bull. Seismol. Soc. Am.*, *71*, 1105–1130, 1981.

Kappel, E. S., and W. B. F. Ryan, Volcanic episodicity on a non-steady state rift valley along northeast Pacific spreading centers: Evidence from Sea MARC I, *J. Geophys. Res.*, *91*, 13,925–13,940, 1986.

Karsten, J. L., S. R. Hammond, E. E. Davis, and R. G. Currie, Detailed geomorphology and neotectonics of the Endeavour segment, Juan de Fuca Ridge: New results from SeaBeam swath mapping, *Geol. Soc. Am. Bull.*, *97*, 213–221, 1986.

Karsten, J. L., J. R. Delaney, J. M. Rhodes, and R. A. Liias, Spatial and temporal evolution of magmatic systems beneath the Endeavour segment, Juan de Fuca Ridge: Tectonic and petrologic constraints, *J. Geophys. Res.,*, *95*, 19,235–19,256, 1990.

Klein, F. W., Hypocenter location program HYPOINVERSE, 1, User's guide to versions 1, 2, 3, 4, *U.S. Geol. Surv. Open File Rep., 78-694*, 1978.

Kong, L. S. L., S. C. Solomon, and G. M. Purdy, Microearthquake characteristics of a mid-ocean ridge along-axis high, *J. Geophys. Res.*, *97*, 1659–1685, 1992.

Kreemer, C., R. Govers, K. P. Furlong, and W. E. Holt, Plate boundary deformation between the Pacific and North America in the Explorer region, *Tectonophysics*, *293*, 225–238, 1998.

Lee, S. M., and S. C. Solomon, Constraints from Sea Beam bathymetry on the development of normal faults on the East Pacific Rise, *Geophys. Res. Lett.*, *22*, 3135–3138, 1995.

McClain, J. S., M. L. Begnaud, M. A. Wright, J. Fondrk, and G. K. Von Damm, Seismicity and tremor in a submarine hydrothermal field: The northern Juan de Fuca Ridge, *Geophys. Res. Lett.*, *20*, 1883–1886, 1993.

Nabelek, J., and X. Ganyuan, Moment-tensor analysis using regional data: Application to the 25 March, 1993, Scotts Mills, Oregon, earthquake, *Geophys. Res. Lett.*, *22*, 13–16, 1995.

Nakamura, Y., A_1 moonquakes: Source distribution and mechanism, *Proc. Lunar Planetary Sci. Conf.*, *9th*(3), 3589–3607, 1978.

Phipps Morgan, J., and Y. J. Chen, Dependence of ridge-axis morphology on magma supply and spreading rate, *Nature*, *364*, 706–708, 1993.

Poupinet, G., W. L. Ellsworth, and J. Frechet, Monitoring velocity variations in the crust using earthquake doublets: An application to the Calaveras fault, California, *J. Geophys. Res.*, *89*, 5719–5731, 1984.

Rohr, K. M. M., Increase of seismic velocities in upper oceanic crust and hydrothermal circulation on the Juan de Fuca plate, *Geophys. Res. Lett.*, *21*, 2163–2166, 1994.

Rohr, K. M. M., and K. P. Furlong, Ephemeral plate tectonics at the Queen Charlotte triple junction, *Geology*, *23*, 1035–1038, 1995.

Rohr, K. M. M., B. Milkereit, and C. J. Yorath, Asymmetric deep crustal structure across the Juan de Fuca Ridge, *Geology*, *16*, 533–537, 1988.

Rosenberg, N. D., J. E. Lupton, D. Kadko, R. Collier, M. D. Lilley, and H. Pak, Estimation of heat and chemical fluxes from a seafloor hydrothermal vent field using radon measurements, *Nature*, *334*, 604–607, 1988.

Scholz, C. H., The critical slip distance for seismic faulting, *Nature*, *336*, 761–763, 1988.

Schultz, A., J. R. Delaney, and R. E. McDuff, On the partitioning of heat flux between diffuse and point source seafloor venting, *J. Geophys. Res.*, *97*, 12,299–12,314, 1992.

Shearer, P. M., Improving local earthquake locations using the L1 norm and waveform cross correlation: Application to the Whittier Narrows, California, aftershock sequence, *J. Geophys. Res.*, *102*, 8269–8283, 1997.

Shearer, P. M., Evidence form a cluster of small earthquakes for a fault at 18 km depth beneath Oak Ridge, southern California, *Bull. Seismol. Soc. Am.*, *88*, 1327–1337, 1998.

Shen, Y., D. W. Forsyth, J. Conder, and L. M. Dorman, Investigation of microearthquake activity following an intraplate teleseismic swarm on the west flank of the southern East Pacific Rise, *J. Geophys. Res.*, *102*, 459–475, 1997.

Shoberg, T., S. Stein, and J. Karsten, Constraints on rift propagation history at the Cobb Offset, Juan de Fuca Ridge, from numerical modeling of tectonic fabric, *Tectonophysics*, *197*, 295–308, 1991.

Slunga, R., S. T. Rögnvaldsson, and R. Bödvarrsson, Absolute and relative locations of similar events with application to microearthquakes in southern Iceland, *Geophys. J. Int.*, *123*, 409–419, 1995.

Small, C., and D. T. Sandwell, An abrupt change in ridge axis gravity with spreading rate, *J. Geophys. Res.*, *94*, 17,383–17,392, 1989.

Sohn, R. A., D. J. Fornari, K. L. Von Damm, J. A. Hildebrand, and S. C. Webb, Seismic and hydrothermal evidence for a cracking event on the East Pacific Rise crest at 9°50′N, *Nature*, *396*, 159–161, 1998a.

Sohn, R. A., J. A. Hildebrand, and S. C. Webb, Postrifting seismicity and a model for the 1993 diking event on the CoAxial segment, Juan de Fuca Ridge, *J. Geophys. Res.*, *103*, 9867–9877, 1998b.

Stahr, F., R. E. McDuff, D. R. Yoerger, A. M. Bradley, and K. Nakamura, Heat flux measurements at the Main Endeavour vent field, Juan de Fuca Ridge, *Eos Trans. AGU*, *81*(48), Fall Meet. Suppl., Abstract OS52I-03., 2000.

Thomson, R. E., J. R. Delaney, R. E. McDuff, D. R. Janecky, and J. S. McClain, Physical characteristics of the Endeavour Ridge hydrothermal plume during July 1988, *Earth Planet. Sci. Lett.*, *111*, 141–154, 1992.

Tivey, M. K., and J. R. Delaney, Growth of large sulfide structures on the Endeavour segment of the Juan de Fuca Ridge, *Earth Planet. Sci. Lett.*, *77*, 303–317, 1986.

Toomey, D. R., S. C. Solomon, G. M. Purdy, and M. H. Murray, Microearthquakes beneath the median valley of the Mid-Atlantic Ridge near 23°N: Hypocenters and focal mechanisms, *J. Geophys. Res.*, *90*, 5443–5458, 1985.

Toomey, D. R., S. C. Solomon, and G. M. Purdy, Microearthquakes beneath the median valley of the Mid-Atlantic Ridge near 23°N: Tomography and tectonics, *J. Geophys. Res.*, *93*, 9093–9112, 1988.

Tréhu, A. M., and S. C. Solomon, Earthquakes in the Orozco transform zone: Seismicity, source mechanisms, and tectonics, *J. Geophys. Res.*, *88*, 8203–8225, 1983.

VanDecar, J. C., and R. S. Crosson, Determination of teleseismic relative phase arrival times using multi-channel cross-correlation and least square, *Bull. Seismol. Soc. Am.*, *80*, 150–169, 1990.

Veirs, S. R., R. E. McDuff, M. D. Lilley, and J. R. Delaney, Locating hydrothermal vents by detecting buoyant, advected plumes, *J. Geophys. Res.*, *104*, 29,239–29,247, 1999.

Waldhauser, F., W. L. Ellsworth, and A. Cole, Slip-parallel seismic lineations on the northern Hayward Fault, California, *Geophys. Res. Lett.*, *26*, 3525–3528, 1999.

Wang, K., J. He, and E. E. Davis, Transform push, oblique subduction resistance, and intraplate stress of the Juan de Fuca plate, *J. Geophys. Res.*, *102*, 661–674, 1997.

White, D. J., and R. M. Clowes, Shallow crustal structure beneath the Juan de Fuca Ridge from 2-D seismic refraction tomography, *Geophys. J. Int.*, *100*, 349–367, 1990.

White, D. J., and R. M. Clowes, Seismic attenuation structure beneath the Juan de Fuca Ridge from tomographic inversion of amplitudes, *J. Geophys. Res.*, *99*, 3043–3056, 1994.

Wilcock, W. S. D., Tidal triggering of microearthquakes on the Juan de Fuca Ridge, *Geophys. Res. Lett.*, *28*, 3999–4002, 2001.

Wilcock, W. S. D., and J. R. Delaney, Mid-ocean ridge sulfide deposits: Evidence for heat extraction from magma chambers or cracking fronts?, *Earth Planet. Sci. Lett.*, *149*, 49–64, 1997.

Wilson, D. S., Confidence intervals for motion and deformation of the Juan de Fuca plate, *J. Geophys. Res.*, *98*, 16,053–16,071, 1993.

Wolfe, C. J., G. M. Purdy, D. R. Toomey, and S. C. Solomon, Microearthquake characteristics and crustal velocity structure at 29°N on the Mid-Atlantic Ridge: The architecture of a slow spreading segment, *J. Geophys. Res.*, *100*, 24,449–24,472, 1995.

S. D. Archer and W. S. D. Wilcock, School of Oceanography, Box 357940, University of Washington, Seattle, WA 98195-7940, USA. (wilcock@ocean.washington.edu)

G. M. Purdy, Lamont-Doherty Earth Observatory, Rte 9W, Palisades, NY 10964, USA. (mpurdy@ldeo.columbia.edu)